ISSN 0915-6364

NATIONAL INSTITUTE FOR FUSION SCIENCE

Cross-section Data Measured at Low Impact Energies for Ar^{q+} Ions on Argon and Neon Targets

X. Ma, H.P. Liu, Z.H. Yang, Y.D. Wang, X.M. Chen, Z.Y. Liu,
I. Murakami and C. Namba

(Received - Mar. 31, 2003)

NIFS-DATA-75 Apr. 2003

TOKI, JAPAN

Cross-section data measured at low impact energies for Ar^{q+} ions on Argon and Neon targets

X. Ma[1,2] H. P. Liu[1], Z. H. Yang[1], Y. D. Wang[1], X. M. Chen[3], Z. Y. Liu[3], I. Murakami[2], C. Namba[2]

1 Institute of Modern Physics, CAS, Lanzhou 730000, China
2 National Institute for Fusion Science, Toki, 509-5292,Japan
3 Lanzhou University, Lanzhou, 730000, China

ABSTRACT

Multiple electron transfer was systematically studied for Ar^{q+} + Ne, and Ar^{q+} + Ar (q = 8, 9, 11, 12) collision systems by using coincidence experimental technique for incident energies from 80keV to 240keV. Various sub-processes of charge exchange were identified and their cross sections were measured in the experiments. The dependencies of cross sections of multiple charge exchange on the charge states of projectiles and the charge states of recoil ions were discussed respectively for the collision systems. Based on the Molecular Coulombic overBarrier Model (MCBM), four steps are suggested in describing HCI-atom collisions: molecularizing of target electron→formation of molecular →dissociation of the molecular and formation of multiply excited scattered ions and recoil ions →autoionizing decay of multiply excited ions. By comparison with experimental data, it was found that the calculated absolute projectile charge changing cross sections are in good agreements with experimental results. It is concluded that the autoionization of multiply excited ions may be the dominant reason of transfer ionization in low energy HCI-atom collisions.

Keywords: Ion-atom collision, charge exchange, cross section, multiply excited states

1. Introduction

The cross section data of charge exchange for ion-atom collisions are of fundamental importance for studying the collision dynamics, these data are also needed in many application fields, like inertial fusion, various kind of plasma studies, ion-implantation, and accelerator applications, etc. In the past decades, many experiments have been carried out for ion-atom collisions [1,2,3]. In most cases, only the relative cross section ratios of different reaction channels were measured, taking an example, the ratio of double to single ionization cross section of He produced in ion He atom collisions, and the projectiles used in the experiments had relative lower charge states. The data of charge exchange cross sections for highly charged projectiles in collision with atoms are still scarce. With the improvement of accelerator technologies, modern ECR ion source [3], EBIT [4], and storage ring [5,6], very highly charged ions, e.g., up to bare uranium, can be obtained in laboratory nowadays, and this opens new fields for studying charge exchange processes.

When a slow, highly charged ion collides with a target atom, the probability for the projectile to capture many electrons is quite large. Besides the dominant one electron capture channel, the reaction channels for two-, three-, four-, and even more electron capture are open. The process becomes quite complicated, for a projectile A^{q+} in collisions with an atom B, the process can be expressed as:

$$A^{q+} + B \rightarrow A^{(q-k)+} + B^{r+} + (r-k)e^{-} \qquad (1)$$

where the projectile A^{q+} finally captures k electron(s) and changes its charge state to $A^{(q-k)+}$, which is called scattered projectile ions. The target atom B loses r electrons and becomes ionized, B^{r+} is the recoil ion. Finally $(r-k)$ electrons are emitted from the collision system. When $r = k$, there is no electron emission and the process is a pure electron capture reaction, while $r > k$, the reaction is called transfer ionization.

In this data compilation, the cross-sections measured for multiple electron transfer as described by equation (1) are reported for $Ar^{(q-k)+}$ (q=8,9,11,12) impact on Ar and Ne targets for impact energies from 80-240 keV.

2. Experimental Technique

The experiment was performed at the atomic physics platform based on the ECR (Electron Cyclotron Resonance) ion source in the Institute of Modern Physics in Lanzhou, coincidence technique was employed between scattered ions and recoil ions in order to identify various reaction channels in reaction (1). The experimental setup has been described elsewhere in detail [7,8]. In figure 1, the experimental setup was sketched and only short description will be given here. The Ar^{q+} ions were provided by the ECR ion source with a terminal voltage from 10 kV to 20 kV, the desired charge state was chosen by a double-focusing dipole magnet (M). Before entering the collision

chamber, the selected projectiles were collimated and defined in size smaller than 0.2×0.3 mm by two sets of four-jaw slits (C1 and C2) which are separated by 600 mm. The ions then crossed the atomic target beam at the center of the chamber, and a differential pumped gas-jet was employed to provide the atomic target beam. The recoil ions produced in the collisions were extracted perpendicular to both the ion beam and atomic beam by an electric field of 50 V/cm (D1), passed through a field-free flight tube, then were accelerated up to 2 kV, and finally detected by a channeltron. The charge states of the recoil ions were determined by measuring the time-of-flight difference between the projectiles and the recoils, while the charge states of the scattered projectiles captured electrons in the collisions were analyzed by a parallel-plate electrostatic deflector (D2) and then detected by a position-sensitive detector (PSD) located 1.0m downstream from the collision center. By using this technique both the charge states of the recoil ions and the scattered projectiles can be recorded in an event list mode at the same time, and a typical two-dimensional spectrum is demonstrated in figure 2.

From the measured two-dimensional map various sub-channels for electron transfer were identified according to the charge conservation in the collisions [7,8]. In Ar^{8+} on Ar collisions, taking for example, 12 reaction channels can be ascribed as following [9,10]:

$$1: Ar^{8+} + Ar \rightarrow Ar^{7+} + Ar^{+}$$

$$2: Ar^{8+} + Ar \rightarrow Ar^{6+} + Ar^{2+}$$

$$3: Ar^{8+} + Ar \rightarrow Ar^{5+} + Ar^{3+}$$

$$4: Ar^{8+} + Ar \rightarrow Ar^{4+} + Ar^{4+}$$

$$5: Ar^{8+} + Ar \rightarrow Ar^{7+} + Ar^{2+} + e^{-}$$

$$6: Ar^{8+} + Ar \rightarrow Ar^{6+} + Ar^{3+} + e^{-}$$

$$7: Ar^{8+} + Ar \rightarrow Ar^{5+} + Ar^{4+} + e^{-}$$

$$8: Ar^{8+} + Ar \rightarrow Ar^{4+} + Ar^{5+} + e^{-}$$

$$9: Ar^{8+} + Ar \rightarrow Ar^{6+} + Ar^{4+} + 2e^{-}$$

$$10: Ar^{8+} + Ar \rightarrow Ar^{5+} + Ar^{5+} + 2e^{-}$$

$$11: Ar^{8+} + Ar \rightarrow Ar^{4+} + Ar^{6+} + 2e^{-}$$

$$12: Ar^{8+} + Ar \rightarrow Ar^{6+} + Ar^{5+} + 3e^{-}$$

In Ar^{12+} on Ar collisions, up to 6 electrons were found finally being captured by the projectile. The electrons are not essentially captured into ground states of the projectile, some of them are in excited states, and forming the so-called hollow ions.

The decay of the multiply excited states via Auger or radiative processes is sensitive to the electron-electron interactions [1,11,12]. The partial cross sections for these charge exchange processes, such as pure electron capture $\sigma^r_{q,q-r}$, phenomenological transfer ionization $\sigma^r_{q,q-k},(k<r)$, projectile charge changing $\sigma_{q,q-k}$, and target ion production σ^r_q, were measured in the experiments.

Additionally, from the 2-dimensional plot, we can identify the multiple collision events and subtract the multiple collision contributions from the measured counts. For example, in the figure 2 the areas labeled with "a", "b", "c", and "d" are contributions from multiple collisions. Label "A" indicates the contribution from background gas N_2 and O_2, respectively.

In figure 3, a typical time of flight spectrum is presented for Ar^{12+} on Ar collisions. The recoils and their charge states are assigned to each peak. N_2^+ and O_2^+ are produced in collisions of ions with background residual gas atoms [8].

3. Definition for Cross-sections

As described in (1), the numbers of electrons captured (k) and ionized (r) in the collisions are fingerprint of different charge transfer processes. The cross sections for various charge transfer channels are labeled by the r and k, and defined as following:

Projectile electron capture cross section: $\sigma_{q,q-k}$, (projectile charge transfer cross section)

Transfer ionization cross section: $\sigma^r_{q,q-k}$,

Recoil ion production cross section: σ^r_q,

Total charge transfer cross section: σ_q,

Pure electron capture cross section: $\sigma^k_{q,q-k}$, (for $\sigma^r_{q,q-k}$ when $r=k$)。

The relations between the above cross sections:

$$\sigma_{q,q-k}=\sum_r \sigma^r_{q,q-k} \tag{2}$$

$$\sigma^r_q=\sum_k \sigma^r_{q,q-k} \tag{3}$$

$$\sigma_q=\sum_k \sigma_{q,q-k}=\sum_k\sum_r \sigma^r_{q,q-k} \tag{4}$$

If $N^r_{q,q-k}$ is the true coincidence counts of a sub-channel in reaction (1) obtained in the experiment, and N_q the total coincidence counts, where the superscript and subscript have the same meaning as defined above for cross sections, the experimental cross sections can be obtained from the following expressions:

$$\sigma^{r}_{q,q-k} = \frac{N^{r}_{q,q-k}}{N_t I_q \eta} \tag{5}$$

$$\sigma_{q,q-k} = \frac{\sum_{r} N^{r}_{q,q-k}}{N_t I_q \eta} \tag{6}$$

$$\sigma^{r}_{q} = \frac{\sum_{k} N^{r}_{q,q-k}}{N_t I_q \eta} \tag{7}$$

$$\sigma_q = \frac{N_q}{N_t I_q \eta} = \frac{\sum_{k}\sum_{r} N^{r}_{q,q-k}}{N_t I_q \eta} \tag{8}$$

$$\sigma^{k}_{q,q-k} = \frac{N^{k}_{q,q-k}}{N_t I_q \eta} \tag{9}$$

where N_t is the areal density of target atoms, I_q the projectile intensity during measurement, η the coincidence detection efficiency of the system.

4. Data Evaluation

In the experiment a gas-jet was employed to supply target beam, it is not easy to get the accurate target density, so we adopted recommended total cross section data of S. Bliman [12,13] to normalize our data. Assuming the recommended cross-section is S_Q, then one gets,

$$S_Q = \frac{N_q}{N_t I_q \eta} = \frac{\sum_{k}\sum_{r} N^{r}_{q,q-k}}{N_t I_q \eta} \tag{10}$$

$$(N_t I_q) = \frac{\sum_{k}\sum_{r} N^{r}_{q,q-k}}{S_Q \eta} \tag{11}$$

Using the above formula, by considering the relation between target density and gas pressure, from the equations (5-9) the following equations can be obtained:

$$\sigma^{r}_{q,q-k} = \frac{N^{r}_{q,q-k}}{\sum_{k}\sum_{r} N^{0,r}_{q,q-k}} S_Q \alpha(p) \tag{12}$$

$$\sigma_{q,q-k} = \frac{\sum_{r} N^{r}_{q,q-k}}{\sum_{k}\sum_{r} N^{r}_{q,q-k}} S_Q \alpha(p) \tag{13}$$

$$\sigma_q^r = \frac{\sum_k N_{q,q-k}^r}{\sum_k \sum_r N_{q,q-k}^r} S_Q \alpha(p) \tag{14}$$

where $\alpha(p)$ is the coefficient which is correspondent to the gas pressure in the upper part of the nozzle of the gas-jet, target density varies for each measurement due to the different pressure [7]. There is simple relation for different pressure, as:

$$\alpha(p) = \frac{P_0}{P} \tag{15}$$

and P_0 is the pressure of the measurement whose data were used for normalization, P the pressure of other measurement.

One can derive the uncertainties for the measured cross sections of $\sigma_{q,q-k}^{0,r}$, $\sigma_{q,q-k}$, σ_q^r as following:

$$\delta\sigma_{q,q-k}^r = \sigma_{q,q-k}^r \cdot \sqrt{(\frac{\delta N_{q,q-k}^r}{N_{q,q-k}^r})^2 + (\frac{\delta N_q}{N_q})^2 + (\frac{\delta\eta}{\eta})^2 + (\frac{\delta\alpha}{\alpha})^2 + (\frac{\delta S_Q}{S_Q})^2} \tag{16}$$

$$\delta\sigma_{q,q-k} = \sigma_{q,q-k} \cdot \sqrt{(\frac{\delta N_{q,q-k}}{N_{q,q-k}})^2 + (\frac{\delta N_q}{N_q})^2 + (\frac{\delta\eta}{\eta})^2 + (\frac{\delta\alpha}{\alpha})^2 + (\frac{\delta S_Q}{S_Q})^2} \tag{17}$$

$$\delta\sigma_q^r = \sigma_q^r \cdot \sqrt{(\frac{\delta N_q^r}{N_q^r})^2 + (\frac{\delta N_q}{N_q})^2 + (\frac{\delta\eta}{\eta})^2 + (\frac{\delta\alpha}{\alpha})^2 + (\frac{\delta S_Q}{S_Q})^2} \tag{18}$$

where δS_Q, $\delta\alpha$, $\delta\eta$, and δN_x are the uncertainties of recommended cross sections, gas pressure, detection efficiency, and peak counts, respectively. In the experiment the data are accumulated for long time and good statistics were obtained. Generally, the relative statistical uncertainties for each sub-processes ranged from 0.3% to 5%. The gas pressure and detection efficiencies were determined with high accuracy. The relative uncertainties of the recommended cross section data are 30%. The last three terms in the equation (16), (17), and (18) are systematic uncertainties. In this data compilation only statistical uncertainties are considered.

5. Theoretical treatment of charge exchange for low energy ion-atom collisions

In order to understand the charge exchange processes, we combined the Molecular Classical over-Barrier Model (MCBM) developed by Niehaus [14,15] with auto-ionization and electron evaporation of multiply excited states. This was described in detail in reference [10], here we only briefly discuss the theoretical treatment. The whole collision process can be divided into four stages, namely, the way-in (when projectile approaches the target atom), molecular formation (the electrons move in the common coulomb potential of the both nuclei), the way-out (the electron captured or re-captured by the projectile and target, respectively.), and the final de-excitation (the multiply excited states decay via electron emission). MCBM describes the first three

stages in great details, but this only concerns the pure electron capture process.

During the way-in, the potential barrier between the two nuclei reduces with the decrease of inter-nuclear distance, when the potential is lower than each electron binding energy, the target electrons are molecularized sequentially. This process continues until the closest nuclear distance reached and is characterized by a string defined by Niehaus, and a combined molecular ion with two nuclear centers is formed (molecular formation). The molecularized electrons move in the common potential of A and B. The molecularizing cross sections σ_m can be obtained for each electron by the ring area defined by the corresponding nuclear distances. Then the projectile and the target atom starts to separate, the potential barrier becomes higher with the increase of the inter-nuclear distance. When the potential height matches the molecularized electron binding energy (Stark shifted), it becomes effective to the electron and the electron can not move over the barrier and only moves in the local potential of A or B, namely, the electron is captured by the projectile A or re-captured by target atom B. The capture probability P is proportional to the phase space density of the final state where the electron is captured and the density may be determined by the degeneracy of the quantum state occupied by the electron in hydrogenic approximation [14]. The capture cross section is then the products of σ_m and P. Till now only pure electron capture was considered in MCBM. The captured electrons are, in most cases, in the excited states and must undergo de-excitation.

The de-excitation was considered only via Auger process (auto-ionization) in Refs. [16,17,18]. In our treatment, the multiply excited states of the projectile undergo Auger decay while the electrons in the multiply excited states of target ions undergo statistical evaporation [7,10]. For projectile auto-ionization, some criterions based on the Auger electron spectra are applied in order to proceed the sequential decay [10,15,17]. To calculate the evaporation probability, one has to get the excitation energy of the system. In our case, the excitation energy were obtained according to the states occupied by the captured electrons based on the MCBM. The values are different from the ones in [19], but more realistic. If one traces each molecularized electrons to its final states in the processes, one can reproduce each possible reaction channel of equation (1). Taking for an example, the 12 sub-channels in the plot of the figure 2 may be reproduced. The processes above discussed can be summarized in the following equation:

$$\begin{aligned} A^{q+} + B \rightarrow (AB)^{q+**} &\rightarrow \mathrm{A}^{(q-s)+**} + B^{s+**} \\ &\rightarrow A^{(q-k)+} + \begin{cases} B^{s+} + (s-k)e^- \\ B^{(s+1)+} + (s+1-k)e^- \\ \vdots \\ B^{(s+n)+} + (s+n-k)e^- \end{cases} \end{aligned} \tag{19}$$

In the following comparisons in the figures, the decay processes considered via auto-ionization are referred as "MCBM + auger" while the decay processes via statistical evaporation are referred as "MCBM + stat.".

6. Comparison with theory and discussions

In figure 4 total projectile charge exchange cross sections σ_q versus the projectile charge states q are plotted for Ar^{q+} on Ar collisions. The dotted line is a linear fit to the experimental data (solid squares), it is obvious that projectile charge exchange cross section σ_q increases linearly with the projectile charge q, which is in good agreement with the theoretical predictions discussed above (see the open squares) [20,21,22,23].

In figure 5, plotted are the projectile charge exchange cross-sections $\sigma_{q,q-k}$ versus final charge states of scattered ions for Ar^{8+} ions in collisions with Ar target atoms. The upper X-axis indicates the number of electrons finally stabilized on the projectile. The cross section $\sigma_{q,q-k}$ decreases as the number of stabilized electrons increase. The theoretical predictions with auto-ionization corrections are in good agreement with experimental data (solid squares). This is also the case for all the Ar^{q+} + Ar collision system. We observed the same results for Ar^{q+} + Ne system, see figure 6 as an example of Ar^{12+} + Ne collisions. Of course the cross section values are smaller for Ne target than for Ar target of the same projectile. This is easy to understand because the outer shell electrons in Ne atom are strongly bounded than in Ar atom.

The partial projectile charge exchange cross sections $\sigma_{q,q-k}$ versus the projectile charge q for Ar^{q+} + Ne collision system are shown in figure 7. The solid symbols represent the experimental data, and the open ones represent calculated data based on the modified MCBM. The cross sections of single electron capture are always dominant and the MCBM describes the cross sections quite well.

Phenomenological transfer ionization cross-sections for one-, three-, and five-electrons finally stabilized on the projectile are shown in figures 8, 9, and 10 as examples, respectively. For the case of one-electron stabilized on the projectile ($k=1$), the $\sigma^r_{q,q-1}$ decreases monotonically with the increase of recoil charge states, here several data points from Danared [24] are also plotted. And the modified MCBM gives reasonably agreement to experimental data. For more than one electrons stabilized on the projectile ($k>1$), the cross-sections $\sigma^r_{q,q-k}(k>1)$ have different distributions, namely, there are maximum at certain recoil charge state. See examples for $k=3$ *and* $k=5$ in figures 9 and 10, respectively. The modified MCBM gives maximum distribution pattern, but the maximum positions are at much higher charge states of the recoils than experimental data. This may be due to the following two reasons, first is that the excitation energies are still overestimated in the statistical model, and second is that argon is medium heavy ions and the radiative decay of multiply excited states are still of importance [7,10,12].

Figures 11-20 show energy dependence of the cross sections. Figures 11-14 show the transfer ionization cross section, $\sigma^r_{q,q-k}$, of Ar^{8+} + Ar collision system. Figure 15

show the recoil ion production cross section, σ_q^r, of Ar^{8+} + Ar collision. Figure 16 show the single electron charge transfer cross section, $\sigma_{q,q-k}^1$, of Ar^{q+} + Ar collision. Figures 17-20 shows the projectile charge transfer cross section, $\sigma_{q,q-k}$, of Ar^{q+} + Ne collision. All cross sections show weak energy dependence.

If we consider the energy dependence in a classic way based on the Bohr-Lindhard model [25], similar to the discussions in previous theoretical treatment section, in electron capture process, the active electron first should escape from the target atom, and then be captured by the projectile. The escaping radius and capture radius are defined in the Bohr-Lindard model [25], in case of slow projectile, namely the projectile velocity is much less than the active electron velocity, the capture radius is much larger than the escaping radius, which means that the escaped electron will be captured certainly by the projectile. The capture cross section is then determined by the escaping radius which is independent of the projectile velocity. As a result, the cross sections for electron capture and other related processes are projectile velocity independent.

On the other hand, if we consider this in a quantum theory, the relative motion between the projectile and the target is much slower than the active electron, similar to Born-Oppenheimer approximation in molecular treatment [26], the total wavefunction of the Schrödinger equation for the collision system can be separated into two independent parts corresponding to nuclear motion and electron motion, respectively. And finally, in the Schrödinger equation, the eigenvalue of the active electron moved in the common potential of the projectile and the target atom appears as an effective potential energy of the nuclei, just like rotational energy of the electron in the hydrogen atom contributes a centrifugal potential to the radial equation. It manifests that the system potential predominates the electron transfer process and consequently, the charge transfer cross sections are independent of the projectile velocities. (From numerical analysis of the solution for the Schrödinger equations, the coupling of the two motions is quite weak, this explains the weak energy dependence of the cross sections.)

In summary, we measured the charge exchange cross-sections in collisions of Ar^{q+} (q=*8, 9, 11, 12*) on Ar and Ne atoms at low impact energies and obtained a set of cross-section data. These data are compiled in the tables of this publication and the details of the table contents are explained below. As for theoretical description of the electron transfer processes at low energies, classical based models meet difficulties in multi-electron transfer, more feasible quantum theories are needed to explain the experimental data.

In this data compilation, all the cross sections are in unit of $10^{-16}cm^2$.

References

1. M. Barat, M. N. Gaboriaud, L. Guillemot, P. Roncin, H. Laurent, and S. Andriamonge, J. Phys. B20(1987)5771

2. J. Ullrich, H. Schmidt-Boecking, Lecture notes in Physics 376, eds. D. Berenyi and G. Hock, 1990, p287
3. K. E. Stiebing, D. Hofmann, H. Schmidt-Boecking, et al., Rev. Sci. Instrum. 63(4), (1992) 2897
4. J. Ullrich, H. Schmidt-Boecking, Phys. Lett. A 125 (1987) 193.
5. X. Ma, Th. Stöhlker, O. Brinzanescu, S. Fritzsche, C. Kozhuharov, T. Ludziejewski, P.H. Mokler, A. Warczak, *Phys. Rev. A64,* (2001) 012704
6. T. Stoehlker, X. Ma, T. Ludziejewski, H. F. Beyer, F. Bosch, O. Brinzanescu, R. W. Dunford, et al., *Phys. Rev. Lett. 86* (2001) 983,
7. Xinwen Ma, Ph. D dissertation, Multiple Electron Transfer in Collisions of Highly Charged Argon Ions on Rare Gas Targets, March, 1998, Institute of Modern Physic, Chinese Academy of Science, Lanzhou, P. R. China
8. MA Xinwen, Liu Huiping, Wang Youde, et.al, Science in China (series A), Vol.41 (1998) 296
9. Xinwen Ma, Chinese Journal of Atomic and Molecular Physics, Vol.15 (1998) 91
10. Xinwen Ma, Huiping Liu, Youde Wang, et. al, Nucl. Instr. Meth. B146 (1998) 67
11. Xinwen Ma, Chinese Journal of Atomic and Molecular Physics, Vol.16 (1999) 203
12. Xinwen Ma, Nuclear Physics Review, Vol.15 (1998) 155
13. S. Bliman, N. Chan-Tung, S. Dousson, et. al., Phys. Rev. A21, 1980, 1856 1862
14. A. Niehaus, J. Phys. B: At: Mol. Phys. 19 (1986) 2925-2937
15. A. Niehaus, Nucl. Instr. Meth. B23 (1987) 17
16. W. Wu, J. P. Giese, Z. Chen, R. Ali, C. L. Cocke, P. Richard, and M. Stoeckli, Phys. Rev. A50 (1994) 502
17. R. Ali, V. Frohne, C. L. Cocke, M. Stoeckli, S. Chen, and M. L. A. Raphaelian, Phys. Rev. Lett. 69 (1992) 2491
18. R. Ali, C. L. Cocke, M. L. A. Raphaelian, and M. Stockli, Phys. ReV. A49 (1994) 3586
19. A. Muller, W. Groh, and E. Salzborn, Phys. Rev. Lett. Vol.51, No.2, (1983) 107
20. Xinwen Ma, Ximeng Chen, Huiping Liu, et.al, XX.ICPEAC, Vienna, Austria, 1997, TH153
21. Xinwen Ma, Huiping Liu, Zhihu Yang, et al., Chinese Journal of Atomic and Molecular Physics, 15 (1998) 112
22. Xinwen Ma, Zhihu Yang, Huiping Liu, et al., Chinese Journal of Atomic and Molecular Physics, 15 (1998) 131
23. Xinwen Ma, Huiping Liu, Youde Wang, et.al, Multiple electron transfer in collisions of highly charged Ar ions on argon atoms, Physica Scripta, T80 (1999) 375.
24. H. Danared, H. andersson, G. Astner, P. Defrance, and S. Rachafi, Phys Scr. 36 (1987) 756
25. N. Bohr and J. Lindhard, K. Dan. Vid. Sel. Mat. Phys. Medd. 1954 , p.28
26. U. Fano and L. Fano, Physics of Atoms and molecules, The university of Chicago press, 1972, p. 434

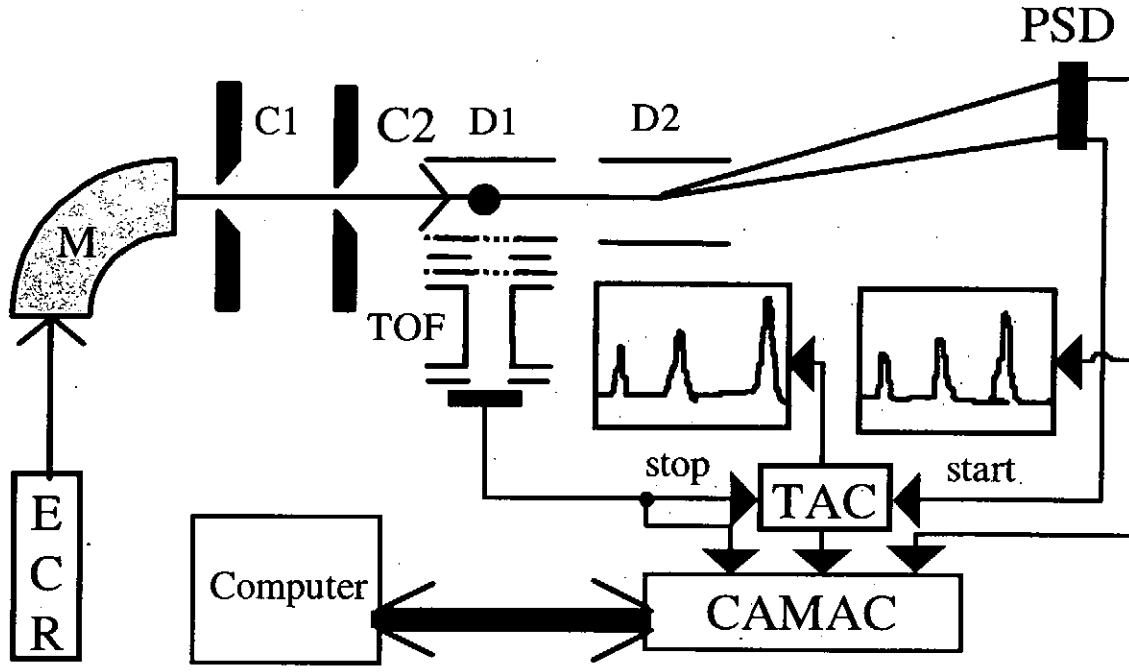

Figure 1. Experimental setup for ion-atom collision studies at the ECR ion source. TOF is the time of flight of recoil ions, PSD the position-sensitive detector, TAC time to analog converter.

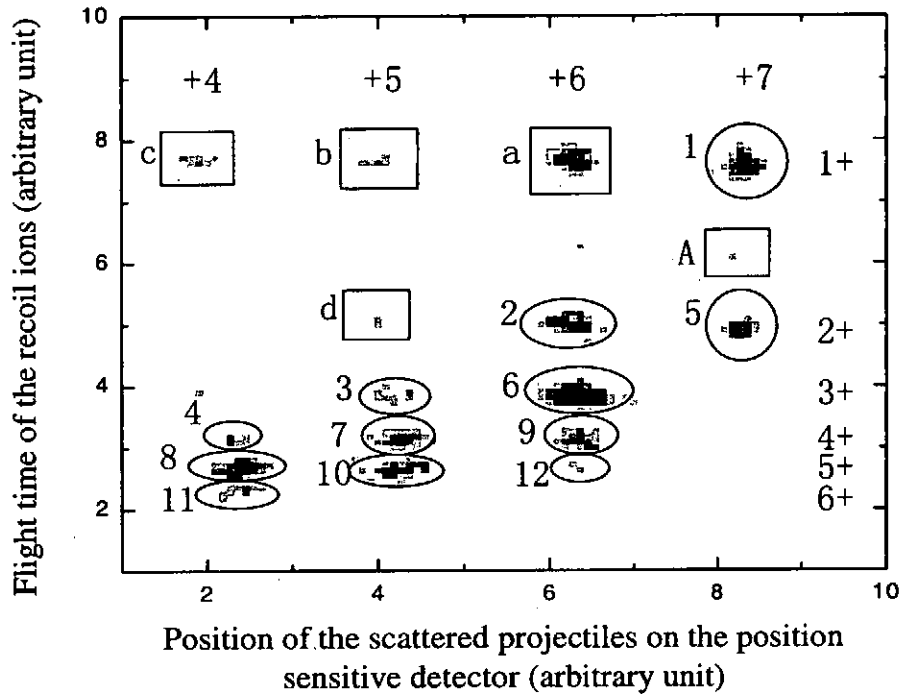

Figure 2. A typical 2-dimension density plot recorded in Ar^{8+} on Ar collisions at impact energy of 104 keV. The vertical axis indicates the charge state of the recoil ions, and the horizontal axis represents the charge state of the scattered ions. For details of the figure see the text.

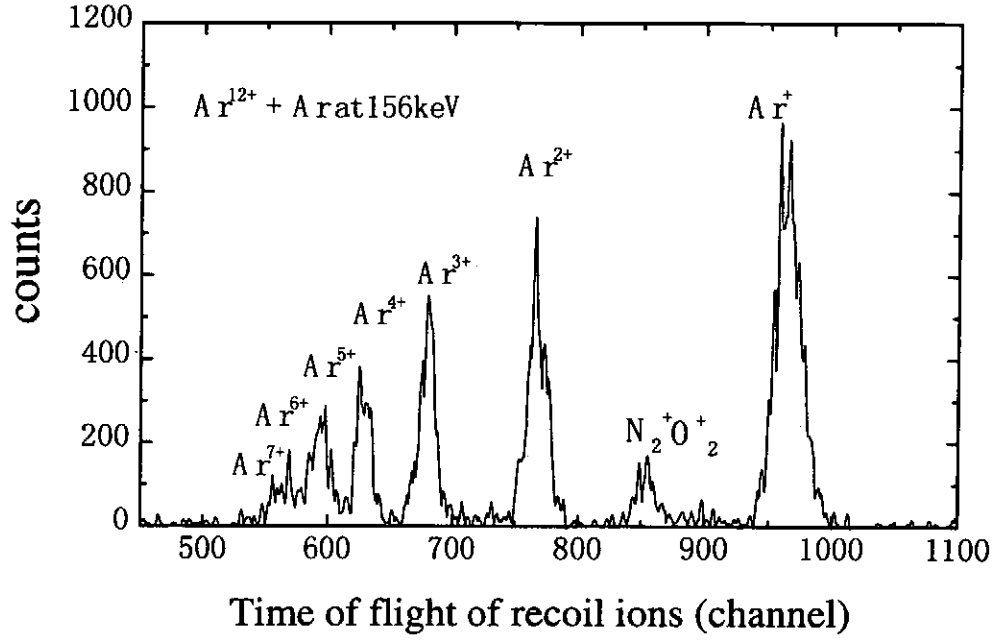

Figure 3. a typical time-of-flight spectrum of recoil ions recorded in Ar^{12+} on Ar collisions. The recoils and their charge states are labeled to each peak. N_2^+ and O_2^+ are the products produced in collisions of ions with residual gas atoms.

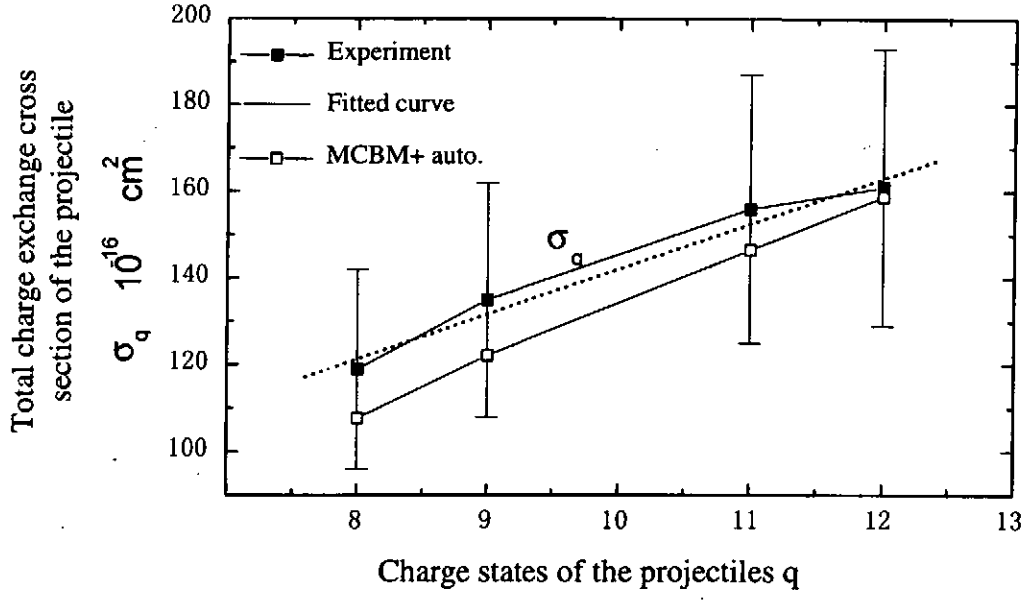

Figure 4. Total projectile charge exchange cross sections versus the projectile charge states q.

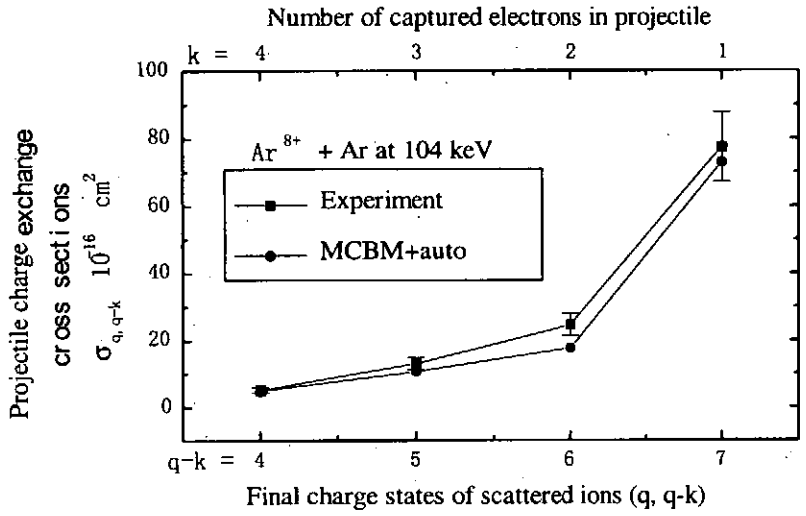

Figure 5. Projectile charge exchange cross sections versus final charge states of scattered ions for Ar^{8+} in collisions with Ar.

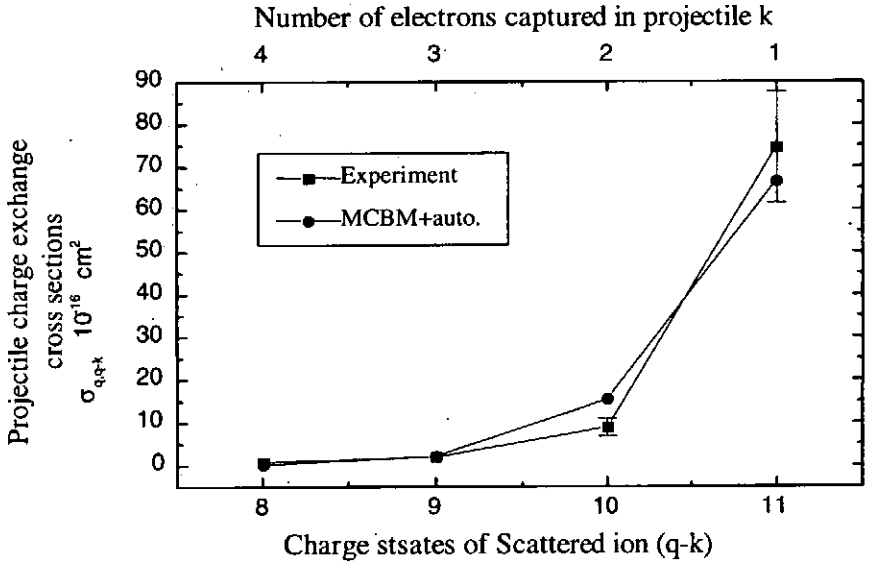

Figure 6. Projectile charge exchange cross sections versus final charge states of scattered ions (number of captured electrons by the projectiles) for Ar12+ in collisions with Ne.

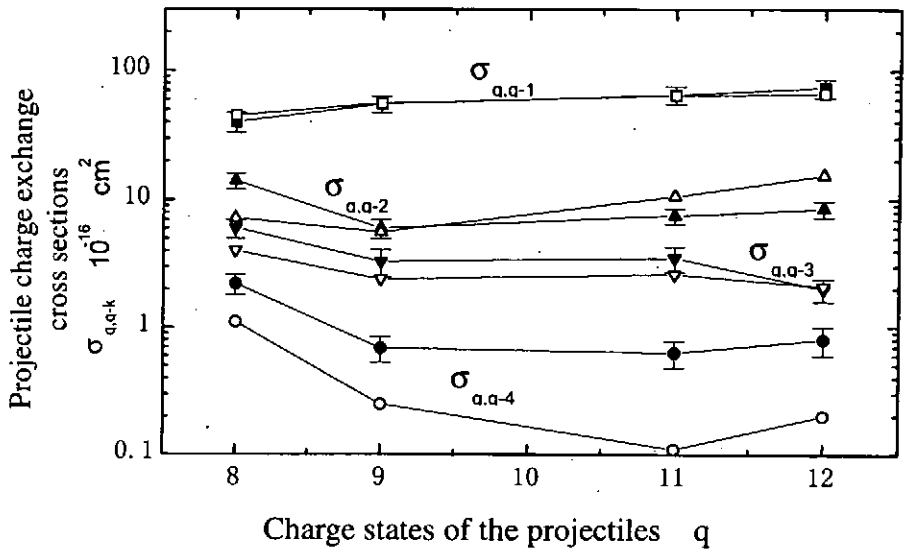

Figure 7. The projectile Charge exchange cross sections σ_q versus the projectile charge q for Ar^{q+} + Ne collision system. The solid symbols represent the experimental data, and the corresponding open symbols are the theoretical data.

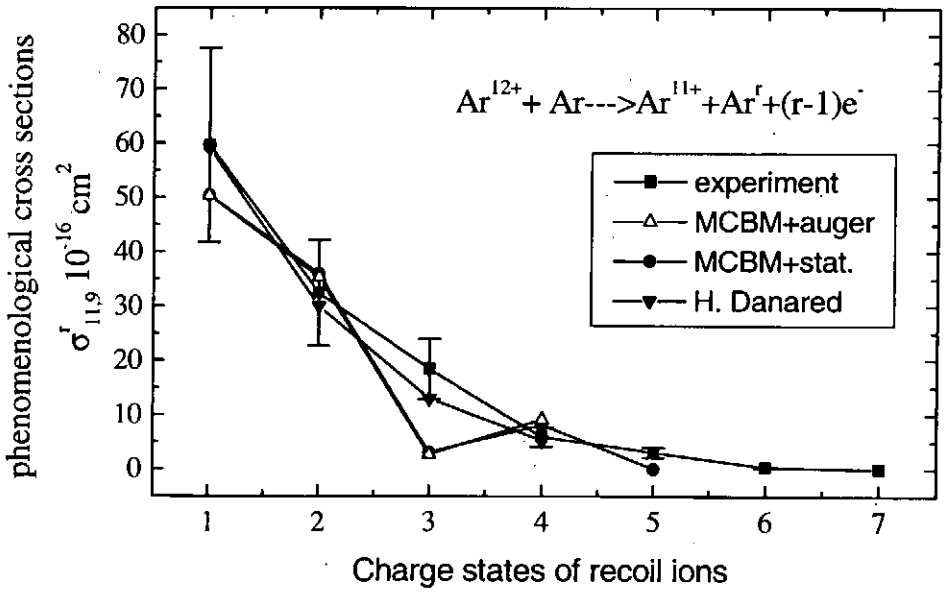

Figure 8. Phenomenological transfer ionization cross sections versus the charge states of recoil ions for one electron stabilized on the projectile in Ar^{12+} on Ar collisions. Experimental data from H. Danared [24] are also presented for comparison (down solid triangles).

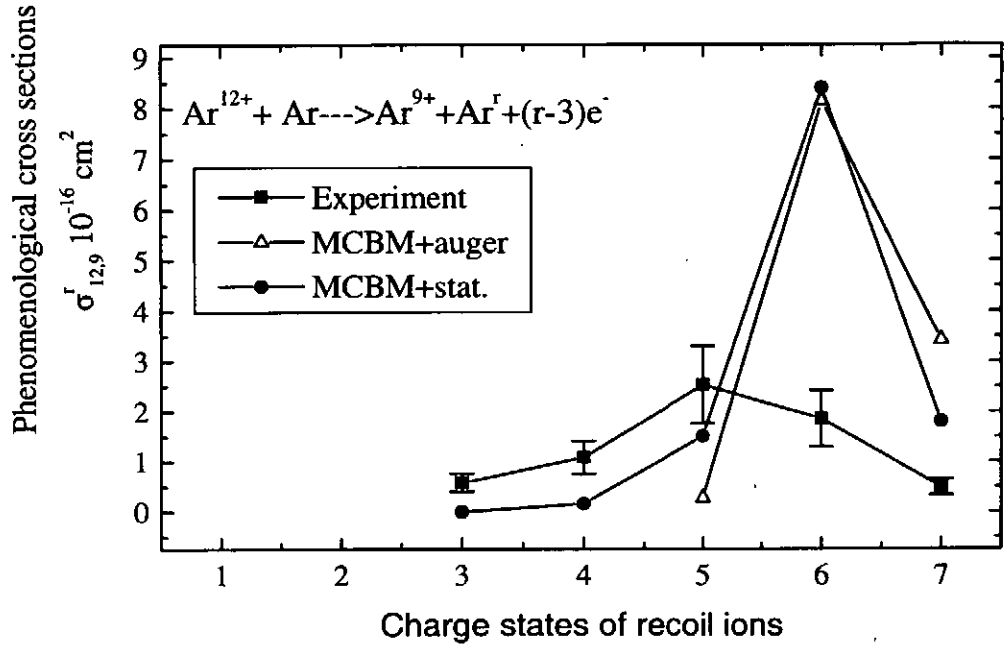

Figure 9. Phenomenological transfer ionization cross sections versus the charge states of recoil ions for three electrons stabilized on the projectile in Ar^{12+} on Ar collisions.

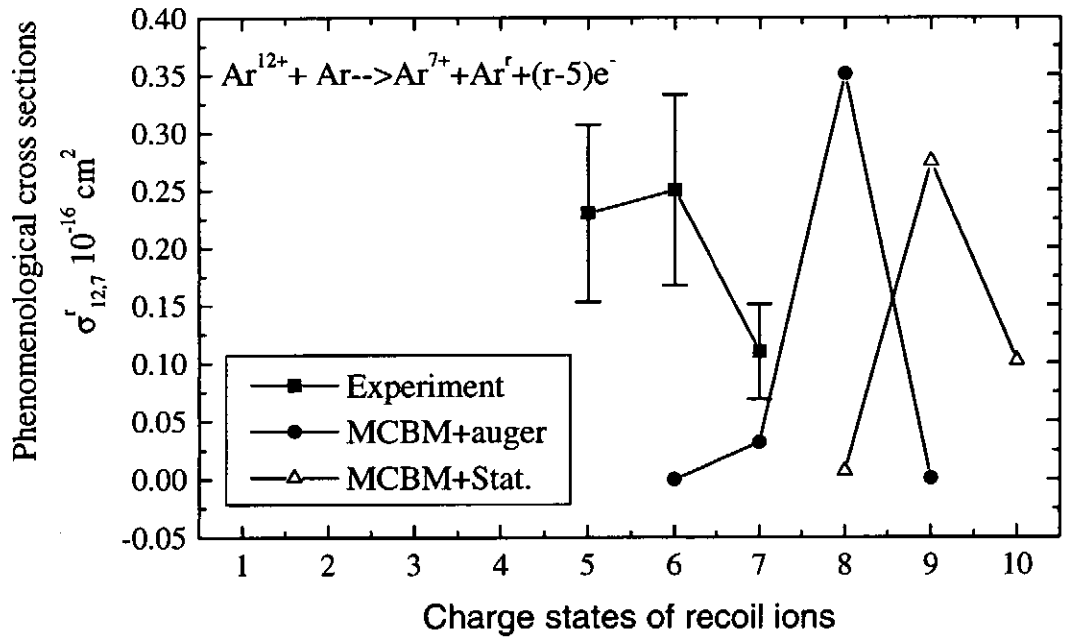

Figure 10. Phenomenological transfer ionization cross sections versus the charge states of recoil ions for five electrons stabilized on the projectile in Ar^{12+} on Ar collisions.

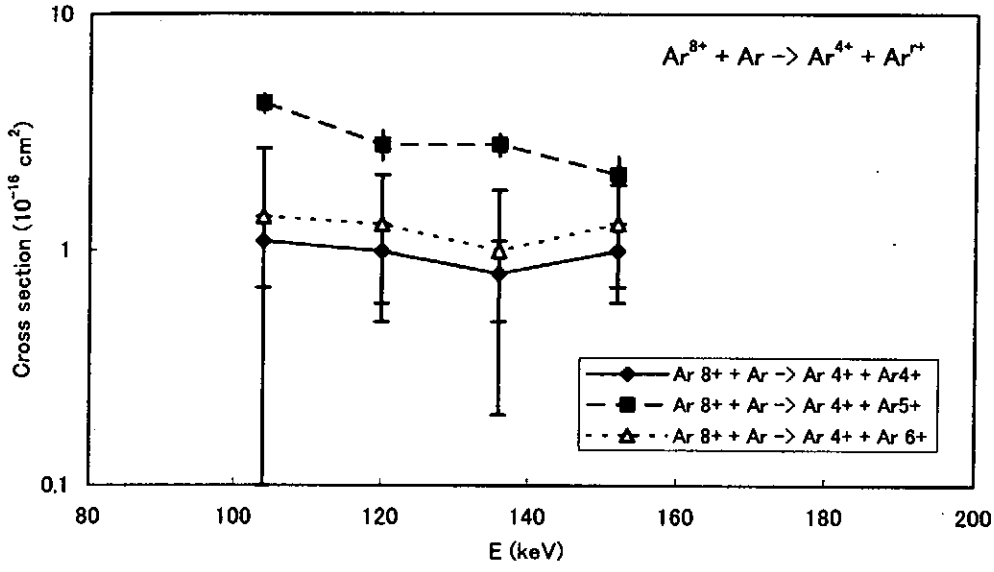

Figure 11. Energy dependence of cross section for Ar^{8+} + Ar -> Ar^{4+} + Ar^{r+} processes.

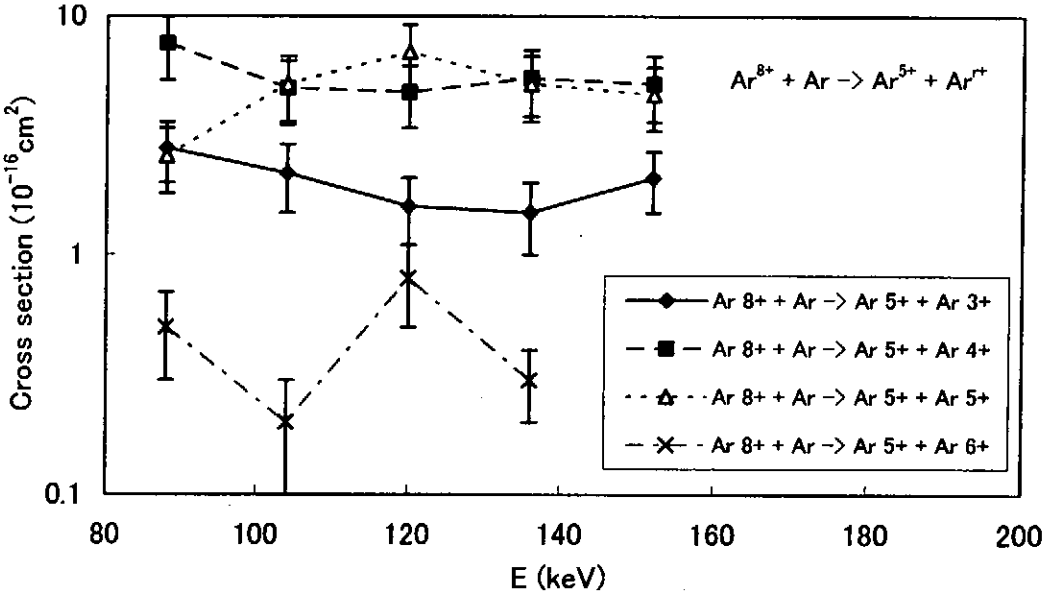

Figure 12. Energy dependence of cross section for Ar^{8+} + Ar -> Ar^{5+} + Ar^{r+} processes.

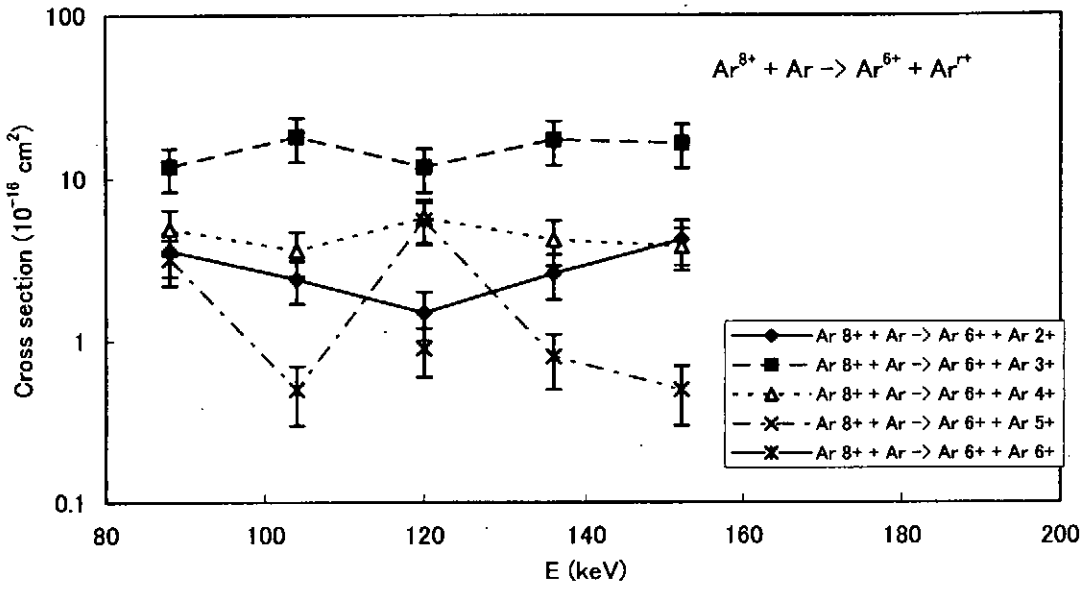

Figure 13. Energy dependence of cross section for Ar^{8+} + Ar -> Ar^{6+} + Ar^{r+} processes.

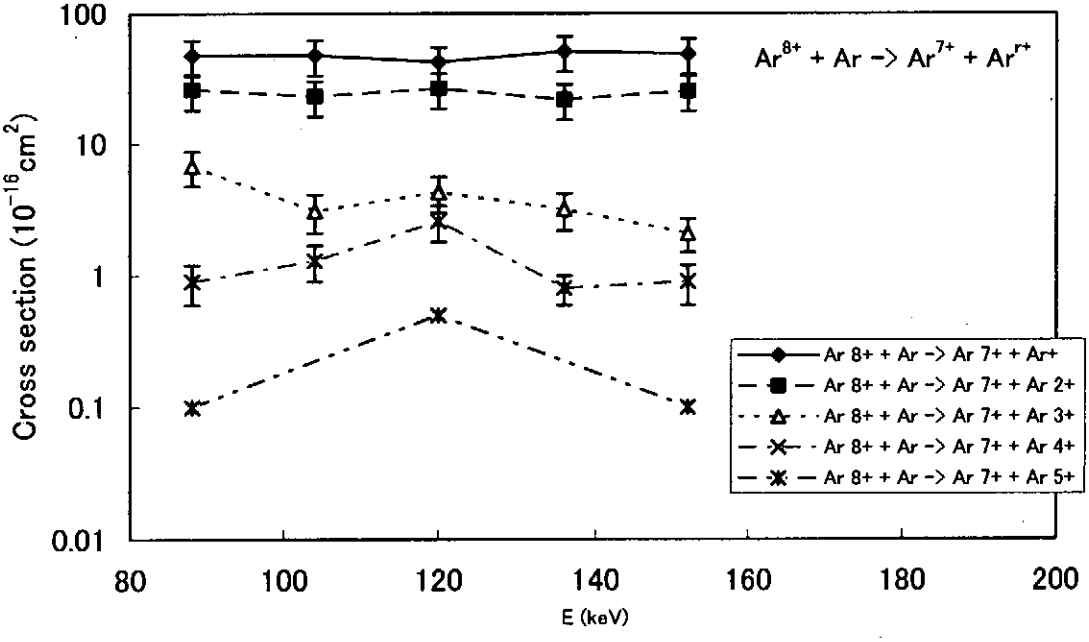

Figure 14. Energy dependence of cross section for Ar^{8+} + Ar -> Ar^{7+} + Ar^{r+} processes.

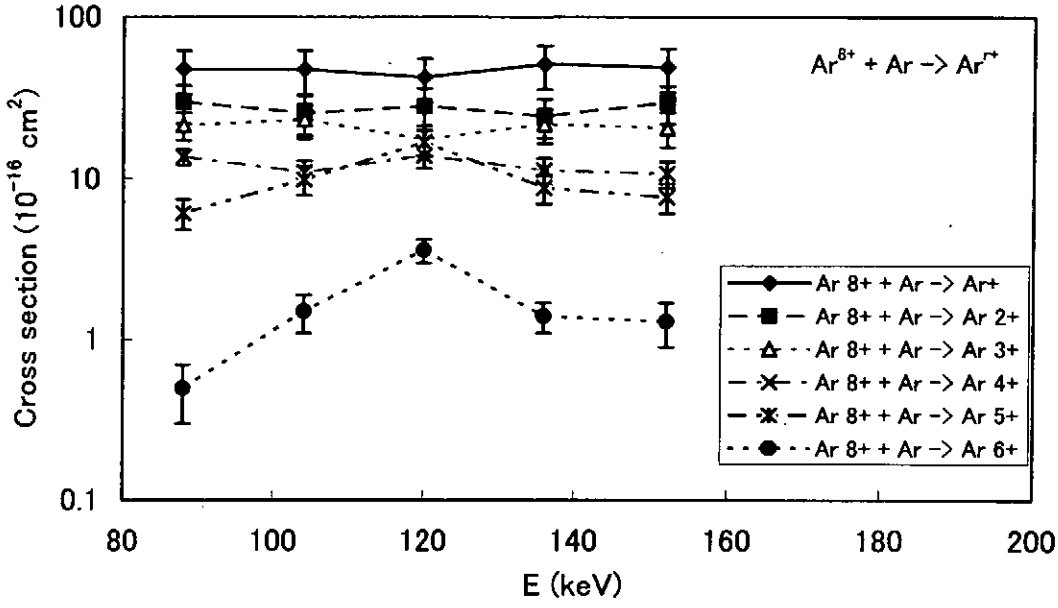

Figure 15. Energy dependence of cross section for recoil ion production processes (Ar^{8+} + Ar -> Ar^{r+}).

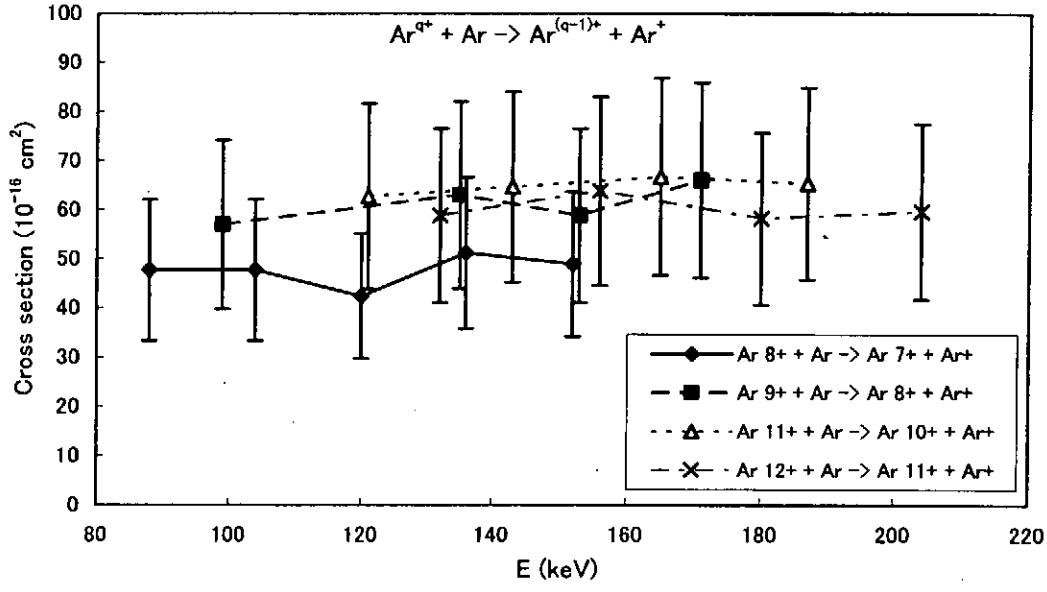

Figure 16. Energy dependence of single electron charge transfer cross sections for Ar^{q+} + Ar collision..

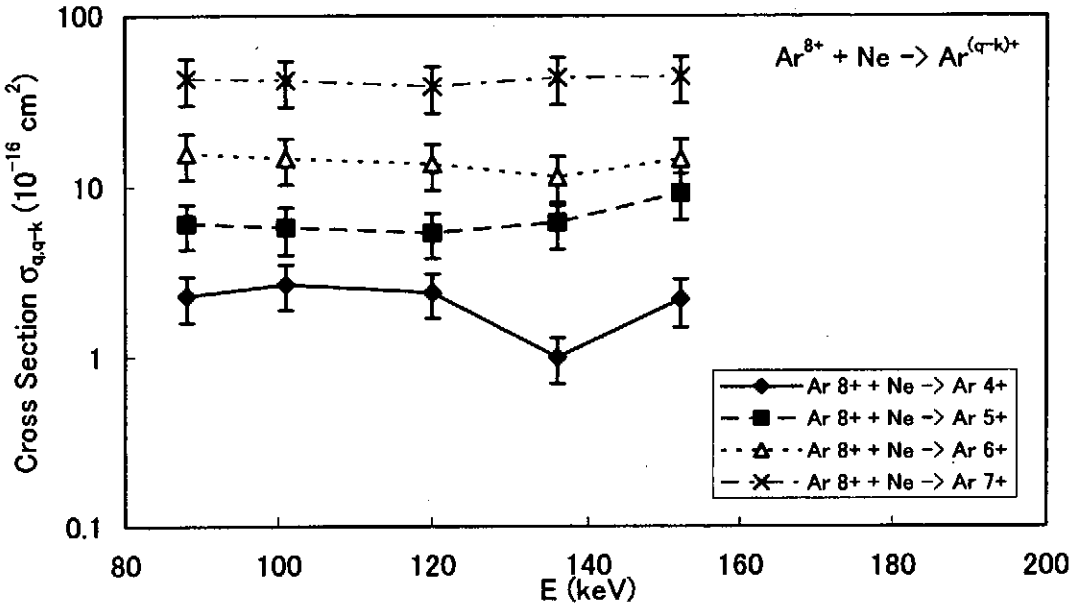

Figure 17. Energy dependence of the charge transfer cross section $\sigma_{q,q-k}$ for projectile Ar^{8+} in collision with Ne.

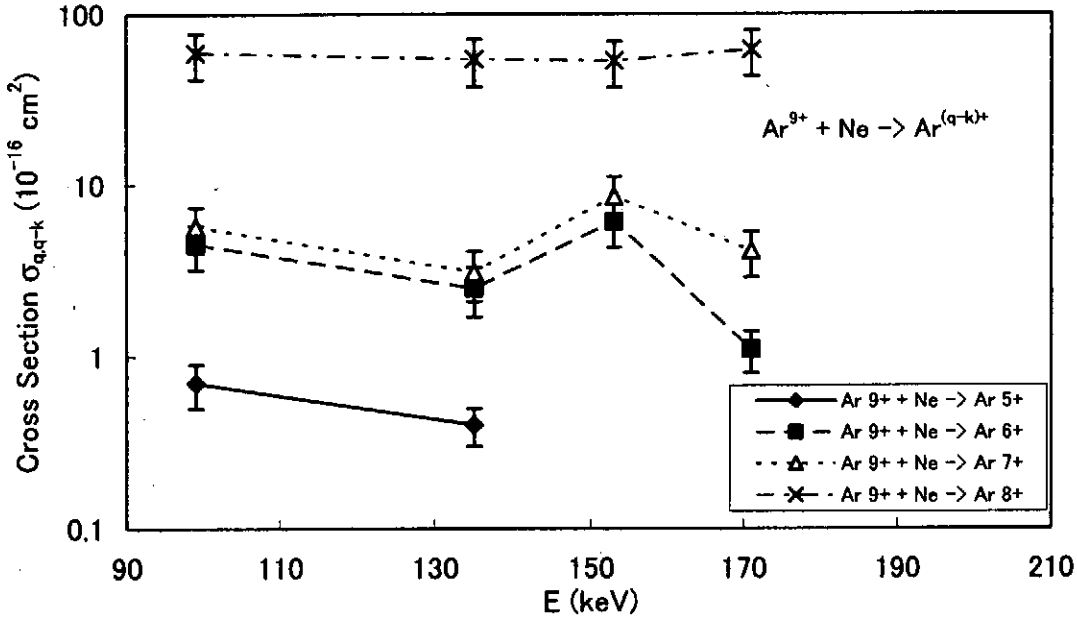

Figure 18. Energy dependence of the charge transfer cross section $\sigma_{q,q-k}$ for projectile Ar^{9+} in collision with Ne.

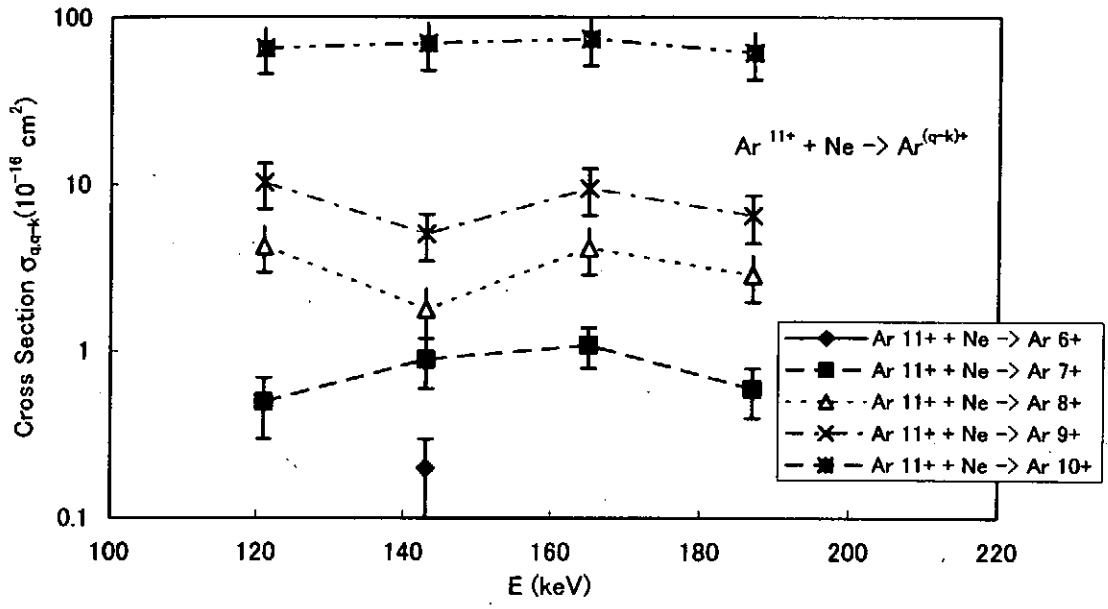

Figure 19. Energy dependence of the charge transfer cross section $\sigma_{q,q-k}$ for projectile Ar^{11+} in collision with Ne.

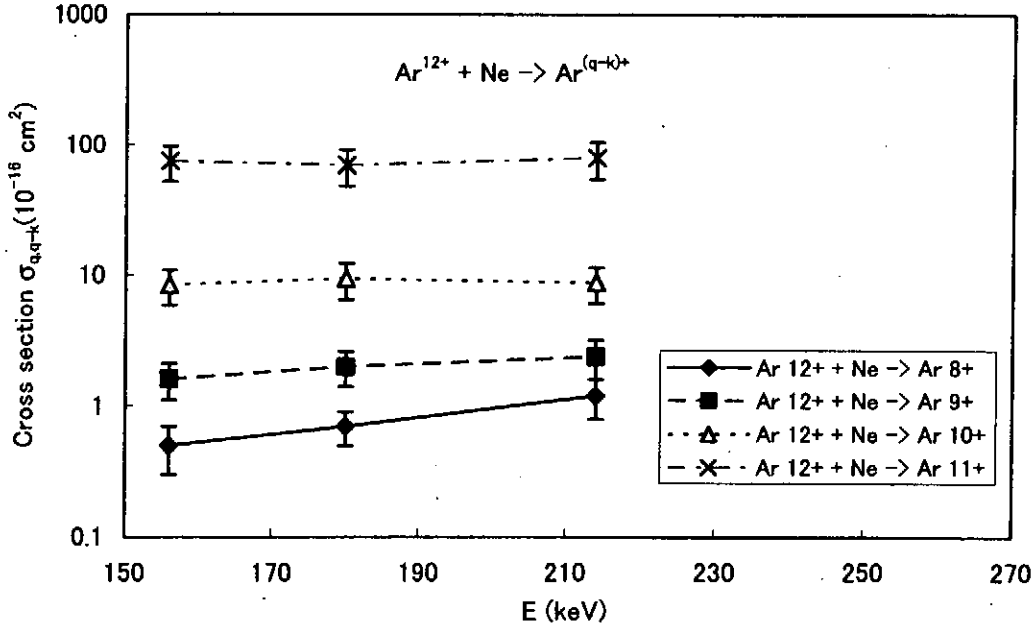

Figure 20. Energy dependence of the charge transfer cross section $\sigma_{q,q-k}$ for projectile Ar^{12+} in collision with Ne.

Configuration of the Table

The tables in this data sheet have the same structure as described below. The first column on the left is the charge states r of recoil ions, the last column on the right is the recoil ion production cross sections σ_q^r, the columns in between are the transfer ionization cross sections $\sigma_{q,q-k}^r$. The first raw in the table is the specification for each column. In some cases, the projectile charge transfer cross sections are given in the last raw of the tables.

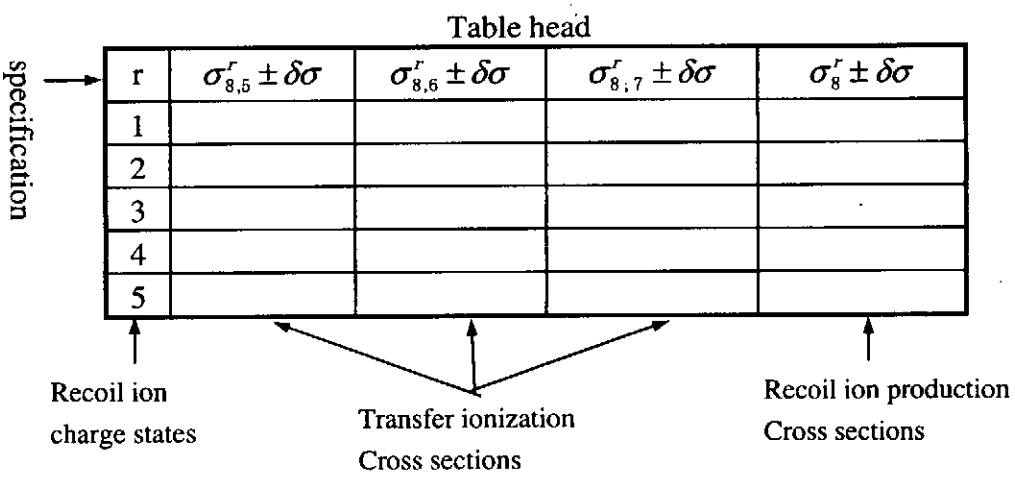

Ar^{8+} + Ar collision system

Table 1 Measured cross sections for Ar^{8+}+Ar at 88KeV

r.	$\sigma^r_{8,5} \pm \delta\sigma$	$\sigma^r_{8,6} \pm \delta\sigma$	$\sigma^r_{8,7} \pm \delta\sigma$	$\sigma^r_{8} \pm \delta\sigma$
1	-	-	47.7±14.3	47.7±14.3
2	-	3.6±1.1	26.1±7.9	29.8±7.9
3	2.8±0.8	11.8±3.5	6.8±2.0	21.4±4.2
4	7.7±2.3	4.9±1.5	0.9±0.3	13.6±1.5
5	2.6±0.8	3.2±1.0	0.2±0.1	6.1±1.3
6	0.5±0.2	-	-	0.5±0.2

Table 2 Measured cross sections for Ar^{8+}+Ar at 104KeV

r.	$\sigma^r_{8,4} \pm \delta\sigma$	$\sigma^r_{8,5} \pm \delta\sigma$	$\sigma^r_{8,6} \pm \delta\sigma$	$\sigma^r_{8,7} \pm \delta\sigma$	$\sigma^r_{8} \pm \delta\sigma$
1	-	-	-	47.7±14.4	47.7±14.4
2	-	-	2.4±0.7	23.2±7.0	25.6±7.0
3	-	2.2±0.7	18.0±5.4	3.1±1. 0	23.3±5.5
4	1.1±0.3	5.0±1.5	3.6±1.1	1.3±0.4	11.0±1.9
5	4.2±1.3	5.2±1.6	0.5±0.2	-	9.9±2.0
6	1.4±0.4	0.2±0.1	-	-	1.5±0.4

Table 3 Measured cross sections for Ar^{8+}+Ar at 120KeV

r.	$\sigma^r_{8,4} \pm \delta\sigma$	$\sigma^r_{8,5} \pm \delta\sigma$	$\sigma^r_{8,6} \pm \delta\sigma$	$\sigma^r_{8,7} \pm \delta\sigma$	$\sigma^r_{8} \pm \delta\sigma$
1	-	-	-	42.4±12.7	42.4±12.7
2	-	-	1.5±0.5	26.6±8.0	28.1±8.0
3	-	1.6±0.5	11.7±3.5	4.3±1.3	17.6±3.8
4	1.0±0.3	4.8±1.4	5.7±1.7	2.6±0.8	14.0±2.4
5	2.8±0.8	7.1±2.1	5.5±1.6	1.6±0.5	16.9±2.9
6	1.3±0.4	0.8±0.3	0.9±0.3	0.6±0.2	3.6±0.6

Table 4 Measured cross sections for Ar^{8+}+Ar at 136KeV

r.	$\sigma^r_{8,4} \pm \delta\sigma$	$\sigma^r_{8,5} \pm \delta\sigma$	$\sigma^r_{8,6} \pm \delta\sigma$	$\sigma^r_{8,7} \pm \delta\sigma$	$\sigma^r_{8} \pm \delta\sigma$
1	-	-	-	51.2±15.4	51.2±15.4
2	-	-	2.6±0.8	21.9±6.6	24.5±6.6
3	-	1.5±0.5	17.2±5.2	3.2±1. 0	21.9±5.3
4	0.8±0.3	5.5±1.7	4.2±1.3	0.8±0.2	11.3±2.1
5	2.8±0.8	5.2±1.6	0.8±0.3	-	8.8±1.8
6	1.0±0.3	0.3±0.1	-	-	1.4±0.3

Table 5 Measured cross sections for Ar^{8+}+Ar at 152KeV

r.	$\sigma^r_{8,4} \pm \delta\sigma$	$\sigma^r_{8,5} \pm \delta\sigma$	$\sigma^r_{8,6} \pm \delta\sigma$	$\sigma^r_{8,7} \pm \delta\sigma$	$\sigma^r_{8} \pm \delta\sigma$
1	-	-	-	48.9±14.7	48.9±14.7
2	-	-	4.2±1.3	25.4±7.6	29.6±7.7
3	-	2.1±0.6	16.4±4.9	2.1±0.6	20.7±5.0
4	1.0±0.3	5.2±1.6	3.8±1.1	0.9±0.3	10.8±2.0
5	2.1±0.6	4.7±1.4	0.5±0.2	0.4±0.1	7.7±1.6
6	1.3±0.4	-	-	-	1.3±0.4

Table 6 Measured cross sections for Ar^{9+}+Ar at 99KeV

r.	$\sigma^r_{9,5} \pm \delta\sigma$	$\sigma^r_{9,6} \pm \delta\sigma$	$\sigma^r_{9,7} \pm \delta\sigma$	$\sigma^r_{9,8} \pm \delta\sigma$	$\sigma^r_{9} \pm \delta\sigma$
1	-	-	-	57.0±17.2	57.0±17.2
2	-	-	1.6±0.5	25.0±7.5	26.7±7.6
3	-	1.7±0.5	6.5±2.0	17.8±5.4	26.0±5.7
4	0.8±0.2	3.2±1.0	5.2±1.6	5.1±1.6	14.2±2.4
5	0.9±0.3	3.2±1.0	3.3±1. 0	-	7.4±1.4
6	1.1±0.3	-	0.5±0.1	-	1.6±0.4
7	0.3±0.1	-	1.0±0.3	-	1.3±0.3

Table 7 Measured cross sections for Ar^{9+}+Ar at 135KeV

r.	$\sigma^r_{9,5} \pm \delta\sigma$	$\sigma^r_{9,6} \pm \delta\sigma$	$\sigma^r_{9,7} \pm \delta\sigma$	$\sigma^r_{9,8} \pm \delta\sigma$	$\sigma^r_{9} \pm \delta\sigma$
1	-	-	-	63.0±19.0	63.0±19.0
2	-	-	2.7±0.8	22.1±6.7	24.8±6.7
3	-	2.7±0.8	8.6±2.6	14.7±4.5	26.0±5.2
4	0.8±0.2	3.3±1.0	2.2±0.7	4.41±1.4	10.7±1.8
5	1.8±0.5	2.3±0.7	0.7±0.2	3.1±1.0	7.9±1.3
6	0.4±0.1	0.9±0.3	0.4±0.1	0.8±0.3	2.5±0.4
7	-	0.4±0.1	-	-	0.4±0.1

Table 8 Measured cross sections for Ar^{9+}+Ar at 153KeV

r.	$\sigma^r_{9,5} \pm \delta\sigma$	$\sigma^r_{9,6} \pm \delta\sigma$	$\sigma^r_{9,7} \pm \delta\sigma$	$\sigma^r_{9,8} \pm \delta\sigma$	$\sigma^r_{9} \pm \delta\sigma$
1	-	-	-	58.8±17.7	58.8±17.7
2	-	-	2.1±0.6	21.3±6.4	23.4±6.5
3	-	2.0±0.6	5.2±1.6	18.6±5.6	25.8±5.9
4	0.6±0.2	1.3±0.4	3.6±1.1	9.6±2.9	15.0±3.1
5	1.0±0.3	2.6±0.8	3.2±1.0	-	6.7±1.3
6	1.0±0.3	2.7±0.8	0.9±0.3	-	4.6±0.9
7	0.3±0.1	0.4±0.1	-	-	0.7±0.2

Table 9 Measured cross sections for Ar^{9+}+Ar at 171KeV

r.	$\sigma^r_{9,5} \pm \delta\sigma$	$\sigma^r_{9,6} \pm \delta\sigma$	$\sigma^r_{9,7} \pm \delta\sigma$	$\sigma^r_{9,8} \pm \delta\sigma$	$\sigma^r_{9} \pm \delta\sigma$
1	-	-	-	66.0±19.9	66.0±19.9
2	-	-	3.8±1.2	23.3±7.0	27.1±7.1
3	-	4.4±1.3	4.6±1.4	15.5±4.7	24.5±5.1
4	1.2±0.4	2.1±0.6	2.4±0.7	5.6±1.7	11.3±2.0
5	1.1±0.3	1.7±0.5	1.8±0.5	-	4.6±0.8
6	0.4±0.1	0.6±0.2	0.4±0.1	-	1.3±0.2
7	0.2±0.1	-	-	-	0.2±0.1

Table 10 Measured cross sections for Ar^{11+}+Ar at 121KeV

r.	$\sigma^r_{11,6} \pm \delta\sigma$	$\sigma^r_{11,7} \pm \delta\sigma$	$\sigma^r_{11,8} \pm \delta\sigma$	$\sigma^r_{11,9} \pm \delta\sigma$	$\sigma^r_{11,10} \pm \delta\sigma$	$\sigma^r_{11} \pm \delta\sigma$
1	-	-	-	-	62.7±18.9	62.7±18.9
2	-	-	-	5.0±1.5	29.3±8.9	34.4±9.0
3	-	-	1.9±0.6	3.0±0.9	18.8±5.7	23.7±5.8
4	-	1.9±0.6	1.3±0.4	5.9±1.8	8.9±2.7	17.9±3.3
5	1.0±0.3	0.5±0.2	1.4±0.4	6.7±2.0	2.3±0.8	11.9±2.2
6	0.7±0.2	0.8±0.3	1.2±0.4	1.6±0.5	-	4.3±0.7
7	-	0.3±0.1	-	0.9±0.3	-	1.2±0.3

Table 11 Measured cross sections for Ar^{11+}+Ar at 143KeV

r.	$\sigma^r_{11,6} \pm \delta\sigma$	$\sigma^r_{11,7} \pm \delta\sigma$	$\sigma^r_{11,8} \pm \delta\sigma$	$\sigma^r_{11,9} \pm \delta\sigma$	$\sigma^r_{11,10} \pm \delta\sigma$	$\sigma^r_{11} \pm \delta\sigma$
1	-	-	-	-	64.6±19.4	64.6±19.4
2	-	-	-	5.4±1.6	29.3±8.8	34.7±9.0
3	-	-	1.7±0.5	5.3±1.6	13.8±4.2	20.7±4.5
4	-	1.4±0.4	1.8±0.6	6.2±1.9	8.8±2.7	18.2±3.3
5	0.4±0.1	0.9±0.3	2.2±0.7	6.2±1.9	3.0±0.9	12.5±2.2
6	0.6±0.2	0.4±0.1	0.9±0.3	1.8±0.6	-	3.6±0.6
7	0.06±0.03	0.2±0.1	0.6±0.2	0.7±0.2	-	1.6±0.3

Table 12 Measured cross sections for Ar^{11+}+Ar at 165KeV

r.	$\sigma^r_{11,6} \pm \delta\sigma$	$\sigma^r_{11,7} \pm \delta\sigma$	$\sigma^r_{11,8} \pm \delta\sigma$	$\sigma^r_{11,9} \pm \delta\sigma$	$\sigma^r_{11,10} \pm \delta\sigma$	$\sigma^r_{11} \pm \delta\sigma$
1	-	-	-	-	66.7±20.1	66.7±20.1
2	-	-	-	4.5±1.4	26.9±8.1	31.4±8.2
3	-	-	1.3±0.4	4.7±1.4	16.4±4.9	22.36±5.2
4	-	0.8±0.3	1.9±0.6	7.0±2.1	7.3±2.2	17.0±3.1
5	0.3±0.1	0.5±0.2	3.0±0.9	7.9±2.4	2.2±0.7	14.0±2.7
6	0.4±0.1	0.3±0.1	1.5±0.4	1.2±0.4	-	3.3±0.6
7	-	0.3±0.1	0.4±0.1	1.0±0.3	-	1.7±0.3

Table 13 Measured cross sections for Ar^{11+}+Ar at 187KeV

r.	$\sigma^r_{11,6} \pm \delta\sigma$	$\sigma^r_{11,7} \pm \delta\sigma$	$\sigma^r_{11,8} \pm \delta\sigma$	$\sigma^r_{11,9} \pm \delta\sigma$	$\sigma^r_{11,10} \pm \delta\sigma$	$\sigma^r_{11} \pm \delta\sigma$
1	-	-	-	-	65.3±19.6	65.3±19.6
2	-	-	-	3.8±1.1	28.4±8.6	32.2±8.6
3	-	-	1.5±0.5	4.4±1.3	14.5±4.4	20.4±4.6
4	-	0.9±0.3	2.3±0.7	6.5±2.0	9.2±2.8	19.0±3.5
5	0.2±0.1	0.7±0.2	2.1±0.7	8.4±2.5	2.5±0.8	13.9±2.7
6	0.3±0.1	0.5±0.2	1.3±0.4	2.3±0.7	0.6±0.2	4.9±0.8
7	-	-	0.4±0.1	-	-	0.4±0.1

Table 14 Measured cross sections for Ar^{12+}+Ar at 132KeV

r.	$\sigma^r_{12,8} \pm \delta\sigma$	$\sigma^r_{12,9} \pm \delta\sigma$	$\sigma^r_{12,10} \pm \delta\sigma$	$\sigma^r_{12,11} \pm \delta\sigma$	$\sigma^r_{12} \pm \delta\sigma$
1	-	-	-	58.8±17.7	58.8±17.7
2	-	-	4.9±1.5	31.0±9.4	35.8±9.5
3	-	1.0±0.3	6.1±1.9	18.9±5.7	26.1±6.0
4	0.5±0.2	1.6±0.5	5.6±1.7	7.6±2.3	15.2±2.9
5	0.5±0.2	2.6±0.8	7.8±2.3	4.1±1.3	15.1±2.8
6	0.4±0.1	2.1±0.7	3.8±1.2	1.2±0.4	7.5±1.4
7	-	0.5±0.1	-	-	0.5±0.1

Table 15 Measured cross sections for Ar^{12+}+Ar at 156KeV

r.	$\sigma^r_{12,7} \pm \delta\sigma$	$\sigma^r_{12,8} \pm \delta\sigma$	$\sigma^r_{12,9} \pm \delta\sigma$	$\sigma^r_{12,10} \pm \delta\sigma$	$\sigma^r_{12,11} \pm \delta\sigma$	$\sigma^r_{12} \pm \delta\sigma$
1	-	-	-	-	63.8±19.2	63.8±19.2
2	-	-	-	4.5±1.4	30.5±9.2	35.1±9.3
3	-	-	1.6±0.5	6.4±1.9	20.3±6.1	28.4±6.4
4	-	2.0±0.6	1.4±0.4	4.8±1.5	6.4±1.9	14.5±2.5
5	0.6±0.2	1.3±0.4	1.2±0.4	8.4±2.5	-	11.5±2.6
6	0.3±0.1	0.6±0.2	1.1±0.3	3.0±0.9	-	5.0±1.0
7	-	0.2±0.1	0.3±0.1	0.4±0.1	-	0.9±0.2

Table 16 Measured cross sections for Ar^{12+}+Ar at 180KeV

r.	$\sigma^r_{12,7} \pm \delta\sigma$	$\sigma^r_{12,8} \pm \delta\sigma$	$\sigma^r_{12,9} \pm \delta\sigma$	$\sigma^r_{12,10} \pm \delta\sigma$	$\sigma^r_{12,11} \pm \delta\sigma$	$\sigma^r_{12} \pm \delta\sigma$
1	-	-	-	-	58.2±17.5	58.2±17.5
2	-	-	-	5.2±1.6	32.5±9.8	37.8±9.9
3	-	-	0.9±0.3	5.7±1.7	17.5±5.3	24.1±5.6
4	-	1.0±0.3	1.8±0.6	5.6±1.7	5.5±1.7	13.8±2.4
5	0.2±0.1	1.0±0.3	2.9±0.9	8.4±2.5	3.2±1.0	15.7±2.9
6	0.1±0.05	0.8±0.2	1.8±0.5	3.7±1.1	1.5±0.5	7.8±1.3
7	0.1±0.04	0.4±0.1	0.5±0.2	0.6±0.2	-	1.6±0.3

Table 17 Measured cross sections for Ar^{12+}+Ar at 204KeV

r.	$\sigma^r_{12,7} \pm \delta\sigma$	$\sigma^r_{12,8} \pm \delta\sigma$	$\sigma^r_{12,9} \pm \delta\sigma$	$\sigma^r_{12,10} \pm \delta\sigma$	$\sigma^r_{12,11} \pm \delta\sigma$	$\sigma^r_{12} \pm \delta\sigma$
1	-	-	-	-	59.6±17.9	59.6±17.9
2	-	-	-	5.2±1.6	32.4±9.8	37.6±9.9
3	-	-	0.6±0.2	6.2±1.9	18.4±5.6	25.2±5.9
4	-	0.5±0.2	1.1±0.3	5.4±1.6	5.9±1.8	12.9±2.5
5	0.2±0.1	1.3±0.4	2.5±0.8	8.3±2.5	3.1±1.0	15.5±2.8
6	0.3±0.1	0.4±0.1	1.9±0.6	4.3±1.3	0.4±0.1	7.1±1.4
7	0.1±0.0	0.2±0.05	0.5±0.2	0.3±0.1	-	1.1±0.2

Ar^{8+}+Ne collision system

Table 18 Measured cross sections for Ar^{8+}+Ne at 88KeV

r.	$\sigma^r_{8,4} \pm \delta\sigma$	$\sigma^r_{8,5} \pm \delta\sigma$	$\sigma^r_{8,6} \pm \delta\sigma$	$\sigma^r_{8,7} \pm \delta\sigma$	$\sigma^r_8 \pm \delta\sigma$
1	-	-	-	31.2±9.4	31.2±9.4
2	-	-	8.2±2.5	9.1±2.8	17.3±3.7
3	-	4.3±1.3	7.0±2.1	2.6±0.8	13.9±2.6
4	2.1±0.6	1.7±0.5	0.4±0.1	-	4.2±0.8
5	0.2±0.1	0.1±0.04	-	-	0.4±0.1
$\sigma_{8,8-k}$	2.3±0.7	6.1±1.8	15.7±4.7	42.9±12.9	67.0±13.9

Table 19 Measured cross sections for Ar^{8+}+Ne at 101KeV

r.	$\sigma^r_{8,4} \pm \delta\sigma$	$\sigma^r_{8,5} \pm \delta\sigma$	$\sigma^r_{8,6} \pm \delta\sigma$	$\sigma^r_{8,7} \pm \delta\sigma$	$\sigma^r_8 \pm \delta\sigma$
1	-	-	-	33.3±10.0	33.3±10.0
2	-	-	5.3±1.6	7.3±2.2	12.6±2.7
3	-	3.7±1.1	8.9±2.7	1.2±0.4	13.8±2.9
4	2.7±0.8	2.1±0.6	0.6±0.2	-	5.3±1.0
$\sigma_{8,8-k}$	2.7±0.8	5.8±1.8	14.7±4.4	41.9±12.6	65.0±13.5

Table 20 Measured cross sections for Ar^{8+}+Ne at 120KeV

r.	$\sigma^r_{8,4} \pm \delta\sigma$	$\sigma^r_{8,5} \pm \delta\sigma$	$\sigma^r_{8,6} \pm \delta\sigma$	$\sigma^r_{8,7} \pm \delta\sigma$	$\sigma^r_8 \pm \delta\sigma$
1	-	-	-	26.88±8.11	26.88±8.11
2	-	-	3.91±1.22	8.48±2.58	12.39±2.85391
3	-	3.6±1.1	7.8±2.4	2.1±0.7	13.4±2.7
4	2.3±0.7	1.8±0.6	1.9±0.6	1.2±0.4	7.1±1.1
5	0.2±0.1	-	-	0.2±0.1	0.4±0.1
$\sigma_{8,8-k}$	2.4±0.7	5.4±1.6	13.6±4.1	38.6±11.7	60.0±12.5

Table 21 Measured cross sections for Ar^{8+}+Ne at 136KeV

r.	$\sigma^r_{8,4} \pm \delta\sigma$	$\sigma^r_{8,5} \pm \delta\sigma$	$\sigma^r_{8,6} \pm \delta\sigma$	$\sigma^r_{8,7} \pm \delta\sigma$	$\sigma^r_{8} \pm \delta\sigma$
1	-	-	-	36.0±11.2	36.0±11.2
2	-	-	4.8±1.5	7.1±2.2	11.8±2.7
3	-	4.2±1.3	6.4±2.0	0.5±0.2	11.1±2.4
4	1.0±0.3	2.1±0.7	0.3±0.1	-	3.3±0.7
$\sigma_{8,8-k}$	1.0±0.3	6.2±1.9	11.4±3.6	43.6±13.5	62.2±14.1

Table 22 Measured cross sections for Ar^{8+}+Ne at 152KeV

r.	$\sigma^r_{8,4} \pm \delta\sigma$	$\sigma^r_{8,5} \pm \delta\sigma$	$\sigma^r_{8,6} \pm \delta\sigma$	$\sigma^r_{8,7} \pm \delta\sigma$	$\sigma^r_{8} \pm \delta\sigma$
1	-	-	-	36.4±10.9	36.4±10.9
2	-	-	5.5±1.7	6.7±2.0	12.2±2.6
3	-	6.2±1.9	9.0±2.7	1.1±0.3	16.3±3.3
4	2.2±0.7	3.0±0.9	-	-	5.2±1.1
$\sigma_{8,8-k}$	2.2±0.7	9.2±2.8	14.5±4.4	44.1±13.3	70.0±14.2

Table 23 Measured cross sections for Ar^{9+}+Ne at 99KeV

r.	$\sigma^r_{9,5} \pm \delta\sigma$	$\sigma^r_{9,6} \pm \delta\sigma$	$\sigma^r_{9,7} \pm \delta\sigma$	$\sigma^r_{9,8} \pm \delta\sigma$	$\sigma^r_{9} \pm \delta\sigma$
1	-	-	-	33.8±10.2	33.8±10.2
2	-	-	1.0±0.3	16.4±4.9	17.4±4.9
3	-	1.9±0.6	2.4±0.7	4.9±1.5	9.2±1.7
4	0.6±0.2	2.1±0.6	2.2±0.7	4.1±1.2	8.9±1.5
5	0.1±0.03	0.5±0.1	0.1±0.04	-	0.7±0.1
$\sigma_{9,9-k}$	0.7±0.2	4.5±1.3	5.7±1.7	59.2±17.8	70.0±17.9

Table 24 Measured cross sections for Ar^{9+}+Ne at 135KeV

r.	$\sigma^r_{9,5} \pm \delta\sigma$	$\sigma^r_{9,6} \pm \delta\sigma$	$\sigma^r_{9,7} \pm \delta\sigma$	$\sigma^r_{9,8} \pm \delta\sigma$	$\sigma^r_{9} \pm \delta\sigma$
1	-	-	-	41.5±12.9	41.5±12.9
2	-	-	1.3±0.4	12.8±4.0	14.1±4.0
3	-	1.2±0.4	1.3±0.4	-	2.5±0.56
4	0.4±0.1	1.0±0.3	0.5±0.2	-	1.8±0.36
5	0.1±0.02	0.3±0.1	-	-	0.4±0.1
$\sigma_{9,9-k}$	0.4±0.1	2.5±0.8	3.1±1.0	54.3±16.9	60.3±16.9

Table 25 Measured cross sections for Ar^{9+}+Ne at 153KeV

r.	$\sigma^r_{9,5} \pm \delta\sigma$	$\sigma^r_{9,6} \pm \delta\sigma$	$\sigma^r_{9,7} \pm \delta\sigma$	$\sigma^r_{9,8} \pm \delta\sigma$	$\sigma^r_{9} \pm \delta\sigma$
1	-	-	-	34.6±10.4	34.6±10.4
2	-	-	1.1±0.3	14.9±4.5	16.1±4.5
3	-	1.4±0.4	3.5±1.0	3.4±1.0	8.2±1.5
4	-	3.5±1.0	3.9±1.2	-	7.4±1.6
5	-	1.3±0.4	-	-	1.3±0.4
6	-	0.5±0.1	-	-	0.5±0.1
7	-	0.5±0.2	-	-	0.5±0.2
$\sigma_{9,9-k}$	-	6.1±1.8	8.5±2.6	52.9±15.9	68.5±16.2

Table 26 Measured cross sections for Ar^{9+}+Ne at 171KeV

r.	$\sigma^r_{9,6} \pm \delta\sigma$	$\sigma^r_{9,7} \pm \delta\sigma$	$\sigma^r_{9,8} \pm \delta\sigma$	$\sigma^r_{9} \pm \delta\sigma$
1	-	-	40.7±12.2	40.7±12.2
2	-	0.6±0.2	16.6±5.0	17.1±5.0
3	0.2±0.1	0.8±0.2	2.8±0.8	3.8±0.9
4	0.6±0.2	1.3±0.4	1.6±0.5	3.6±0.7
5	0.2±0.1	1.4±0.4	-	1.6±0.4
$\sigma_{9,9-k}$	1.1±0.3	4.1±1.2	61.6±18.5	66.8±18.5

Table 27 Measured cross sections for Ar^{11+}+Ne at 187KeV

r.	$\sigma^r_{11,7} \pm \delta\sigma$	$\sigma^r_{11,8} \pm \delta\sigma$	$\sigma^r_{11,9} \pm \delta\sigma$	$\sigma^r_{11,10} \pm \delta\sigma$	$\sigma^r_{11} \pm \delta\sigma$
1	-	-	-	41.3±12.8	41.3±12.8
2	-	-	0.9±0.3	12.4±3.9	13.4±3.9
3	-	0.2±0.1	2.3±0.7	6.5±2.1	9.0±2.2
4	0.4±0.1	0.8±0.3	2.0±0.6	1.2±0.4	4.4±0.8
5	0.3±0.1	1.4±0.4	1.4±0.4	0.3±0.1	3.3±0.6
6	-	0.51±0.17	-	-	0.51±0.17
$\sigma_{11,11-k}$	0.6±0.2	2.9±0.9	6.6±2.1	61.6±19.1	71.8±19.3

Table 28 Measured cross sections for Ar^{11+}+Ne at 143KeV

r.	$\sigma^r_{11,6} \pm \delta\sigma$	$\sigma^r_{11,7} \pm \delta\sigma$	$\sigma^r_{11,8} \pm \delta\sigma$	$\sigma^r_{11,9} \pm \delta\sigma$	$\sigma^r_{11,10} \pm \delta\sigma$	$\sigma^r_{11} \pm \delta\sigma$
1	-	-	-	-	47.7±14.8	47.7±14.8
2	-	-	-	0.8±0.3	12.7±4.0	13.5±4.0
3	-	-	0.1±0.03	1.8±0.6	8.2±2.5	10.0±2.6
4	-	0.7±0.2	0.6±0.2	1.4±0.4	1.3±0.4	4.0±0.7
5	0.2±0.1	0.2±0.1	1.1±0.3	1.0±0.3	-	2.5±0.5
$\sigma_{11,11-k}$	0.2±0.1	0.9±0.3	1.8±0.6	5.1±1.6	69.8±21.7	77.7±21.7

Table 29 Measured cross sections for Ar^{11+}+Ne at 121KeV

r.	$\sigma^r_{11,7} \pm \delta\sigma$	$\sigma^r_{11,8} \pm \delta\sigma$	$\sigma^r_{11,9} \pm \delta\sigma$	$\sigma^r_{11,10} \pm \delta\sigma$	$\sigma^r_{11} \pm \delta\sigma$
1	-	-	-	44.7±13.4	44.7±13.4
2	-	-	3.1±0.9	15.2±4.6	18.3±4.7
3	-	0.2±0.04	3.7±1.1	5.0±1.5	8.9±1.9
4	0.2±0.04	1.5±0.5	2.2±0.7	-	3.8±0.8
5	0.3±0.1	2.6±0.8	1.3±0.4	-	4.2±0.9
$\sigma_{11,11-k}$	0.5±0.2	4.3±1.3	10.3±3.1	65.0±19.5	80.0±19.8

Table 30 Measured cross sections for Ar^{11+}+Ne at 165KeV

r.	$\sigma^r_{11,7} \pm \delta\sigma$	$\sigma^r_{11,8} \pm \delta\sigma$	$\sigma^r_{11,9} \pm \delta\sigma$	$\sigma^r_{11,10} \pm \delta\sigma$	$\sigma^r_{11} \pm \delta\sigma$
1	-	-	-	50.3±15.6	50.3±15.6
2	-	-	1.2±0.4	15.1±4.7	16.3±4.7
3	-	0.6±0.2	3.2±1.0	8.6±2.7	12.4±2.9
4	0.5±0.2	1.4±0.4	2.1±0.6	0.4±0.1	4.4±0.8
5	0.6±0.2	1.9±0.6	1.8±0.6	-	4.2±0.8
6	-	0.3±0.1	1.5±0.5	-	1.8±0.5
$\sigma_{11,11-k}$	1.1±0.3	4.2±1.3	9.6±3.0	74.4±23.1	89.4±23.3

Table 31 Measured cross sections for Ar^{12+}+Ne at 156KeV

$\sigma^r_{12} \pm \delta\sigma$	$\sigma^r_{12,8} \pm \delta\sigma$	$\sigma^r_{12,9} \pm \delta\sigma$	$\sigma^r_{12,10} \pm \delta\sigma$	$\sigma^r_{12,11} \pm \delta\sigma$	$\sigma^r_{12} \pm \delta\sigma$
1	-	-	-	45.4±13.6	45.4±13.6
2	-	-	2.9±0.9	19.8±6.0	22.7±6.0
3	-	0.2±0.1	2.5±0.8	8.8±2.6	11.5±2.7
4	0.2±0.1	0.3±0.1	1.7±0.5	0.6±0.2	2.7±0.5
5	0.4±0.1	0.6±0.2	1.3±0.4	-	2.3±0.5
6	-	0.4±0.1	-	-	0.4±0.1
$\sigma_{12,12-k}$	0.5±0.2	1.6±0.5	8.4±2.5	74.5±22.4	85.0±22.5

Table 32 Measured cross sections for Ar^{12+}+Ne at 214KeV

r.	$\sigma^r_{12,8} \pm \delta\sigma$	$\sigma^r_{12,9} \pm \delta\sigma$	$\sigma^r_{12,10} \pm \delta\sigma$	$\sigma^r_{12,11} \pm \delta\sigma$	$\sigma^r_{12} \pm \delta\sigma$
1	-	-	-	47.4±14.7	47.4±14.7
2	-	-	1.8±0.6	19.7±6.1	21.5±6.2
3	-	1.2±0.4	3.6±1.1	12.1±3.8	16.9±4.0
4	0.7±0.2	0.8±0.3	2.2±0.7	-	3.7±0.8
5	0.6±0.2	0.5±0.2	1.1±0.4	-	2.1±0.4
$\sigma_{12,12-k}$	1.2±0.4	2.4±0.8	8.8±2.7	79.1±24.6	91.5±24.7

Table 33 Measured cross sections for Ar^{12+}+Ne at 180KeV

r.	$\sigma^r_{12,8} \pm \delta\sigma$	$\sigma^r_{12,9} \pm \delta\sigma$	$\sigma^r_{12,10} \pm \delta\sigma$	$\sigma^r_{12,11} \pm \delta\sigma$	$\sigma^r_{12} \pm \delta\sigma$
1	-	-	-	43.2±13.4	43.2±13.4
2	-	-	2.0±0.6	20.0±6.2	22.0±6.3
3	-	0.2±0.1	4.2±1.3	5.7±1.8	10.1±2.2
4	0.3±0.1	0.6±0.2	2.2±0.7	0.8±0.3	3.9±0.8
5	0.4±0.1	1.1±0.4	1.0±0.3	-	2.5±0.5
6	0.1±0.03	-	-	-	0.1±0.03
$\sigma_{12,12-k}$	0.7±0.2	2.0±0.6	9.4±2.9	69.7±21.6	81.8±21.8

Recent Issues of NIFS-DATA Series

NIFS-DATA-49 S. Sasaki, M. Goto, T. Kato and S. Takamura,
Line Intensity Ratios of Helium Atom in an Ionizing Plasma: Oct. 1998

NIFS-DATA-50 I. Murakami, T. Kato and U. Safronova,
Spectral Line Intensities of NeVII for Non-equilibrium Ionization Plasma Including Dielectronic Recombination Processses: Jan. 1999

NIFS-DATA-51 Hiro Tawara and Masa Kato,
Electron Impact Ionization Data for Atoms and Ions -up-dated in 1998-: Feb. 1999

NIFS-DATA-52 J.G. Wang, T. Kato and I. Murakami,
Validity of n^{-3} Scaling Law in Dielectronic Recombination Processes: Apr. 1999

NIFS-DATA-53 J.G. Wang, T. Kato and I. Murakami,
Dielectronic Recombination Rate Coefficients to Excited States of He from He^{+}: Apr. 1999

NIFS-DATA-54 T. Kato and E. Asano,
Comparison of Recombination Rate Coefficients Given by Empirical Formulas for Ions from Hydrogen through Nickel: June 1999

NIFS-DATA-55 H.P. Summers, H. Anderson, T. Kato and S. Murakami,
Hydrogen Beam Stopping and Beam Emission Data for LHD: Nov. 1999

NIFS-DATA-56 S. Born, N. Matsunami and H. Tawara,
A Simple Theoretical Approach to Determine Relative Ion Yield (RIY) in Glow Discharge Mass Spectrometry (GDMS): Jan. 2000

NIFS-DATA-57 T. Ono, T. Kawamura, T. Kenmotsu, Y. Yamamura,
Simulation Study on Retention and Reflection from Tungsten Carbide under High Fluence of Helium Ions: Aug. 2000

NIFS-DATA-58 J.G. Wang, M. Kato and T. Kato,
Spectra of Neutral Carbon for Plasma Diagnostics: Oct. 2000

NIFS-DATA-59 Yu. V. Ralchenko, R. K. Janev, T. Kato, D.V. Fursa, I. Bray and F.J. de Heer
Cross Section Database for Collision Processes of Helium Atom with Charged Particles.
I. Electron Impact Processes: Oct. 2000

NIFS-DATA-60 U.I. Safronova, C. Namba, W.R. Johnson, M.S. Safronova,
Relativistic Many-Body Calculations of Energies for n = 3 States in Aluminiumlike Ions: Jan. 2001

NIFS-DATA-61 U.I. Safronova, C. Namba, I. Murakami, W.R. Johnson and M.S. Safronova,
E1,E2, M1, and M2 Transitions in the Neon Isoelectronic Sequence: Jan. 2001

NIFS-DATA-62 R. K. Janev, Yu.V. Ralchenko, T. Kenmotsu,
Unified Analytic Formula for Physical Sputtering Yield at Normal Ion Incidence: Apr. 2001

NIFS-DATA-63 Y. Itikawa,
Bibliography on Electron Collisions with Molecules: Rotational and Vibrational Excitations, 1980-2000 Apr. 2001

NIFS-DATA-64 R.K. Janev, J.G. Wang and T.Kato,
Cross Sections and Rate Coefficients for Charge Exchange Reactions of Protons with Hydrocarbon Molecules: May 2001

NIFS-DATA-65 T. Kenmotsu, Y. Yamamura, T. Ono and T. Kawamura,
A New Formula of the Energy Spectrum of Sputtered Atoms from a Target Material Bombarded with Light Ions at Normal Incidence: May 2001

NIFS-DATA-66 I. Murakami, U. I. Safronova and T. Kato,
Dielectronic Recombination Rate Coefficients to Excited States of Be-like Oxygen: May 2001

NIFS-DATA-67 N. Matsunami, E. Hatanaka, J. Kondoh, H. Hosaka, K. Tsumori, H. Sakaue and H. Tawara,
Secondary Charged Particle Emission from Proton Conductive Oxides by Ion Impact; July 2001

NIFS-DATA-68 R.K. Janev, J.G. Wang, I. Murakami and T. Kato,
Cross Sections and Rate Coefficients for Electron-Impact Ionization of Hydrocarbon Molecules: Oct. 2001

NIFS-DATA-69 S. Zou, T. Kato, I. Murakami,
Charge Exchange Recombination Spectroscopy of Li III Ions for Fusion Plasma Diagnostics: Oct. 2001

NIFS-DATA-70 I. Murakami, T. Kato, A. Igarashi, M. Imai, Y. Itikawa, D. Kato, M. Kimura, T. Kusakabe, K. Moribayashi, T. Morishita, K. Motohashi, L. Pichl
AMDIS and CHART update (I): Oct. 2002

NIFS-DATA-71 S. Zou, L. Pichl, M. Kimura and T. Kato
Total, Partial and Differential Ionization Cross Sections in Proton-hydrogen Collisions at Low Energy: Jan. 2003

NIFS-DATA-72 M. Hayashi
Bibliography of Electron and Photon Cross Sections with Atoms and Molecules Published in the 20th Century – Argon –: Jan. 2003

NIFS-DATA-73 J. Horacek, K. Houfek, M. Cizek, I. Murakami and T. Kato
Rate Coefficients for Low-Energy Electron Dissociative Attachment to Molecular Hydrogen: Feb. 2003

NIFS-DATA-74 M. Hayashi
Bibliography of Electron and Photon Cross Sections with Atoms and Molecules Published in the 20th Century – Carbon Dioxide –: Apr. 2003

NIFS-DATA-75 X. Ma, H.P. Liu, Z.H. Yang, Y.D. Wang, X.M. Chen, Z.Y. Liu, I. Murakami and C. Namba
Cross-section Data Measured at Low Impact Energies for Ar^{q+} Ions on Argon and Neon Targets. Apr. 2003